REPORT DOCUMENTATION PAGE

AFRL-SR-AR-TR-05-

0006

Public reporting burden for this collection of information is estimated to average 1 hour per response, including the time for reviewing gathering and maintaining the data needed, and completing and reviewing the collection of information. Send comments regarding of information, including suggestions for reducing this burden to Washington Headquarters Service, Directorate for Information Oper 1215 Jefferson Davis Highway, Suite 1204, Arlington, VA 22202-4302, and to the Office of Management and Budget, Paperwork Reduction Project (0704-0188) Washington, DC 20503.
PLEASE DO NOT RETURN YOUR FORM TO THE ABOVE ADDRESS.

1. REPORT DATE (DD-MM-YYYY) 19/05/2004	2. REPORT TYPE Final Report	3. DATES COVERED (From - To) FEB 2002 - Jun 2003

4. TITLE AND SUBTITLE	5a. CONTRACT NUMBER
ACTIVE CONTROL OF SECONDARY FLOW IN ENGINE INLETS	
	5b. GRANT NUMBER F49620-02-1-0123
	5c. PROGRAM ELEMENT NUMBER
6. AUTHOR(S) Sullivan, John P.	5d. PROJECT NUMBER
	5e. TASK NUMBER
	5f. WORK UNIT NUMBER

7. PERFORMING ORGANIZATION NAME(S) AND ADDRESS(ES) Purdue University Sponsored Program Services 610 Purdue Mall West Lafayette, IN 47907-2040	8. PERFORMING ORGANIZATION REPORT NUMBER

9. SPONSORING/MONITORING AGENCY NAME(S) AND ADDRESS(ES) Air Force Office of Scientific Research 4015 Wilson Blvd Room 713 NA Arlington, VA 22203-1954	10. SPONSOR/MONITOR'S ACRONYM(S) AFOSR
	11. SPONSORING/MONITORING AGENCY REPORT NUMBER

12. DISTRIBUTION AVAILABILITY STATEMENT
Unclassified Unlimited DISTRIBUTION STATEMENT A
Approved for Public Release
Distribution Unlimited

20050112 014

13. SUPPLEMENTARY NOTES

14. ABSTRACT

As the next generation of unmanned aerial vehicles (UAV) and unmanned combat aerial vehicles (UCAV) are being developed, the need for highly compact inlet diffusers is increasing quickly. In order to design and evaluate such inlets, additional flow property measurement techniques need to be brought to bear on the situation. The use of pressure-sensitive paint (PSP) and seven-hole pressure probes on these designs will expand the knowledge and understanding of flow properties and behavior involved in highly compact inlet diffusers. The purpose of this thesis is to evaluate the use of PSP and seven-hole pressure probe in evaluating inlet diffusers.

15. SUBJECT TERMS

16. SECURITY CLASSIFICATION OF:			17. LIMITATION OF ABSTRACT	18. NUMBER OF PAGES	19a. NAME OF RESPONSIBLE PERSON John P. Sullivan
a. REPORT	b. ABSTRACT	c. THIS PAGE			19b. TELEPONE NUMBER (Include area code) (765) 494-3344
UU	UU	UU		84	

Standard Form 298 (Rev. 8-98)
Prescribed by ANSI-Std Z39-18

Final Report

ACTIVE CONTROL OF SECONDARY FLOW IN ENGINE INLETS

AFOSR F49620-02-1-0123

Purdue 531 1282-0171

John Sullivan
Purdue University
School of Aeronautics & Astronautics
315 N. Grant St. Grissom Hall
West Lafayette, IN 47907-2023

1. Introduction

As the next generation of unmanned aerial vehicles (UAV) and unmanned combat aerial vehicles (UCAV) are being developed, the need for highly compact inlet diffusers is increasing quickly. In order to design and evaluate such inlets, additional flow property measurement techniques need to be brought to bear on the situation. The use of pressure-sensitive paint (PSP) and seven-hole pressure probes on these designs will expand the knowledge and understanding of flow properties and behavior involved in highly compact inlet diffusers. The purpose of this thesis is to evaluate the use of PSP and seven-hole pressure probe in evaluating inlet diffusers.

The design of traditional engine inlets has been fairly simple and straightforward. Aircraft propulsion systems use S-ducts to move air from a wing or fuselage intake to the engine. Such examples of aircraft with S-ducts are the Boeing 727, Lockheed-Martin F-16 and the Boeing F-18, Wellborn [?]. A properly designed inlet diffuser will efficiently decelerate the flow with minimal flow distortion and total pressure losses.

The next generation of UAVs and UCAVS are expected to be small, stealthy aircraft. The dominant factor driving the design is the size and shape of the engine inlets. The size and weight of the aircraft demands a very compact diffuser. The stealth or low-observability (LO) requirement involves obscuring the high temperature blades at the engine face from detection from all angles forward of the aircraft. In order to meet these LO requirements, the inlet diffuser needs to have more curvature and higher centerline offsets.

As the diffusers in these aircraft become more compact and have greater offsets, longitudinal and circumferential static pressure gradients are generated that produce strong secondary flows along the circumference of the walls as shown in Figure 1. These secondary flows lead to excessive pressure fluctuations at the engine face, which in severe instances can lead to engine stall.
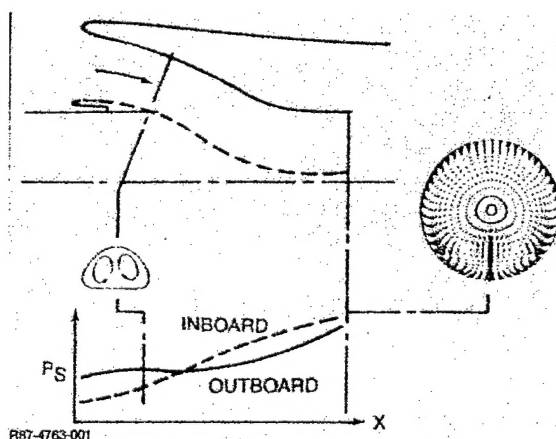

Figure 1. Example of Secondary Flow in an S-Duct, Tindell [?]

In order to develop methods and control systems to mitigate these pressure fluctuations and flow distortions, a more detailed pressure mapping of the flow field is needed. PSP will enable the pressure mapping of the entire duct wall and provide more detail of the flow field than an array of conventional pressure taps. A seven-hole probe will be used to

measure the total pressure loss and velocity field at the engine face. With these two techniques, a better understanding of the flow field in inlet diffusers can be developed.

2. Secondary Flow in S-Ducts

1. Background

For developing flow in a curved pipe, there are two distinct regions. The first is the central region of the flow which is not influence by viscosity, the inviscid core, and the second is a thin boundary layer, Berger et al. [?]. As the flow enters the bend, there is a pressure gradient oriented toward the center of curvature. This azimuthal pressure gradient balances the centrifugal force generated as the fluid moves around the bend.

This produces a secondary flow in the system where the slower boundary layer is moving inward and the faster inviscid core is moving outward. Figures 2 and 3 show work done at Purdue University with developing flow in a 90 degree, constant-area circular pipe bend, Davis [?].

As the flow continues around the bend (moving from the bottom of the image to the top), the azimuthal pressure increases, and the fluid begins to move around the circumference of the duct as seen in Figure 2(a) and 3. As the boundary layer grows and slows down, eventually the azimuthal pressure gradient increases enough that the secondary flow lifts off and a pair of counter-rotating vortices form along the inside surface of the bend. At this time an inviscid core occupies the upper portion of the cross-section of the duct and a disturbed region occupies the lower portion of the duct. The twin vortices can be seen in Figure 2(b) and 3, Davis [?]. These vortices greatly distort the flow field and lead to large losses in total pressure in the lower section and large pressure gradients across the exit of the duct.

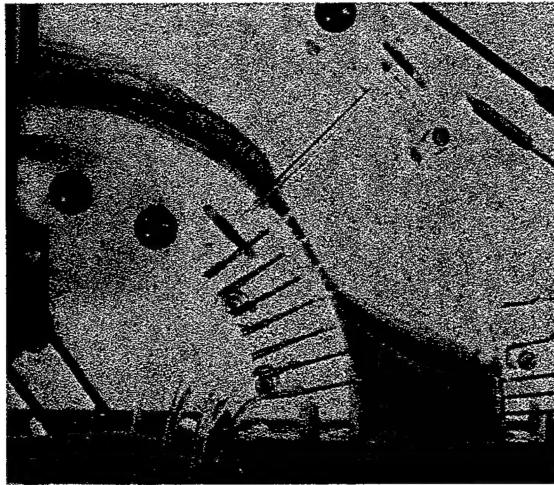(a)   (b)
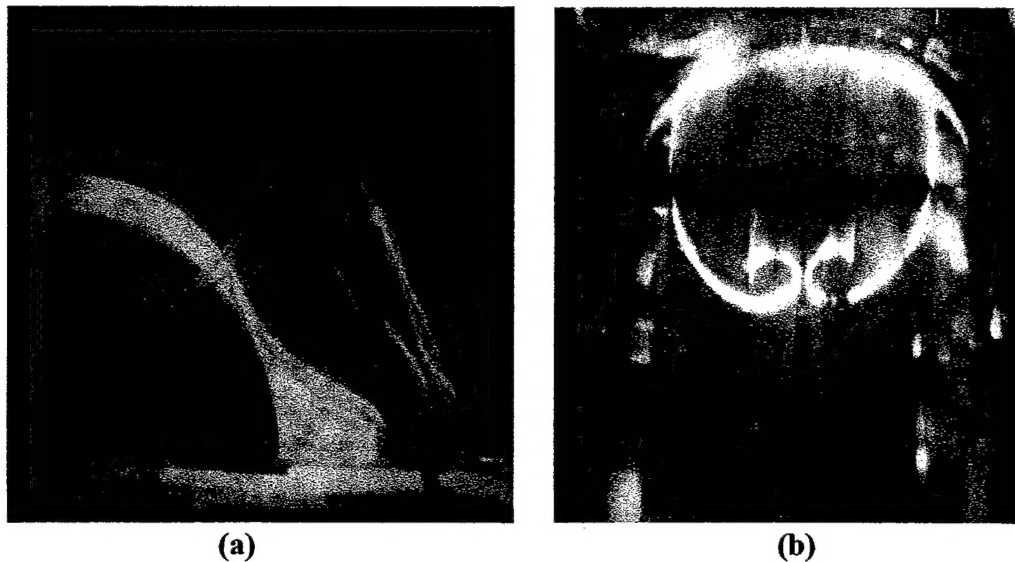
Figure 2. Azimuthal pressure gradients and twin vortices in a 90 degree bend, Davis [?]

Figure 3. Azimuthal pressure gradients and twin vortices formation in a 90 degree bend, Davis [?]

In Figure 4, Davis also showed that in a 45 degree-45 degree S-duct, that the twin vortices form in the first bend and are then amplified in the second bend [?]. This leads to a large disturbed region in the lower region of the duct at the exit plane.

Figure 4. 45 degree-45 degree S-duct showing twin vortex formation and separation, Davis [?]

For highly-curved, highly-offset inlet diffusers, the formation of this flow phenomena is effected due to the longitudinal pressure gradient set up by the diffusion process, Tindell [?]. This adverse pressure gradient increases the growth rate at which the boundary layer. The increased energy loss in the boundary layer can cause the vortex pair to separate from the lower wall of the duct. In some cases, it forms a separated region where the vortices detach and then reattach downstream whereas in more severe cases, the vortices can remain detached.

The existence of these vortices and attempts to control their effects at the duct exit has been studied through work performed by Anderson et al. at NASA Lewis [?], Whitelaw

et al. at Imperial College of Science [?,?], Wellborn et al. at Iowa State University [?,?], and Reichert et al. at NASA Lewis [?].

A flow visualization performed by Wellborn and Reichert using surface oil patterns, Figure 5, shows a separated flow region in a diffusing S-duct, Wellborn [?]. Figure 5 shows that the vortices separate from the lower wall and then reattach downstream.
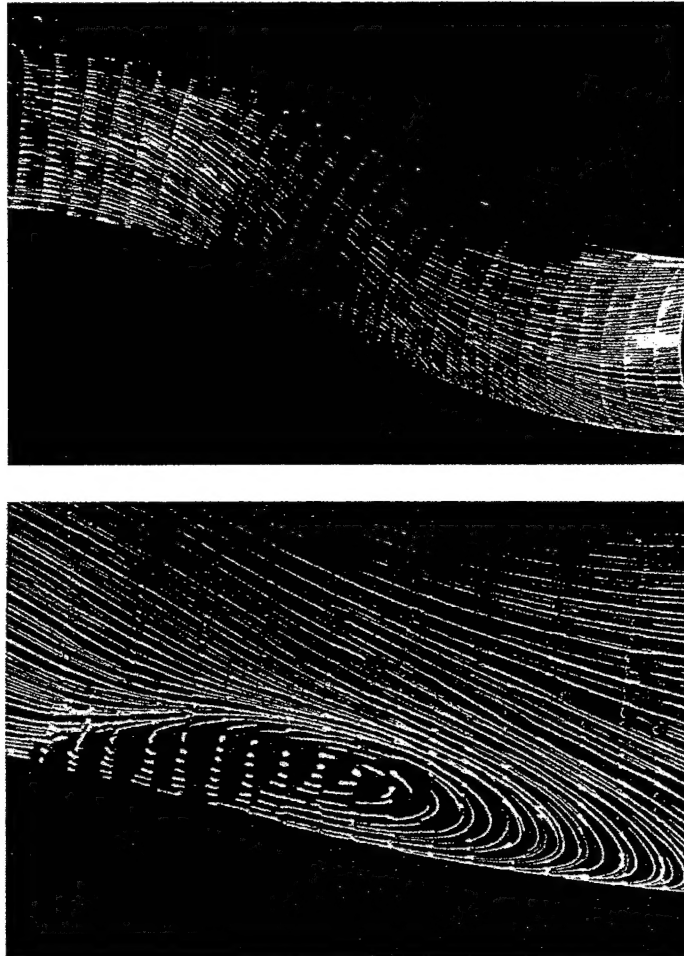
Figure 5. Oil Flow Visualization of a Vakili-type S-Duct, Wellborn [?]

2. Previous Work

Over the last 30 years, there has been extensive work done to describe and quantify the flow properties and behavior in diffusing S-ducts. In order to provide common geometries to study this flow, mathematically defined duct shapes have been developed. The three principle parameters that define the duct shape are the ratio of length to engine face diameter (L/D_e), the ratio of inlet area to exit area (A_i/A_e), and the vertical offset (Z_{offset}). The centerline definition is driven by the L/D_e and the Z_{offset} of the centerline.

There are two predominant shapes used, the RAE/M2129 shaped duct and 30 degree-30 degree S-duct used by Vakili [?].

The RAE/M2129, henceforth referred to as the M2129, shaped duct was developed by the Royal Aerospace Establishment to be used in optimizing intake geometry design, Whitelaw [?]. The centerline shape is defined as follows:

$$\frac{z_{cl}}{L} = \frac{Z_{off}}{2}\left[1 - \cos(\pi\frac{x_{cl}}{L})\right]$$ (1)

The area distribution is defined as:

$$R = R_t + (R_e - R_t)\left[3\left(1 - \frac{x_{cl}}{L}\right)^4 - 4\left(1 - \frac{x_{cl}}{L}\right)^3 + 1\right]$$ (2)

The centerline of the Vakili-type duct is defined as:
For $0 \le \theta \le \theta_{max}/2$

$$x_{cl} = R\sin\theta$$ (3)

$$z_{cl} = R\cos\theta - R$$ (4)

For $\theta_{max}/2 \le \theta \le \theta_{max}$

$$x_{cl} = 2R\sin\frac{\theta_{max}}{2} - R\sin(\theta_{max} - \theta)$$ (5)

$$z_{cl} = 2R\cos\frac{\theta_{max}}{2} - R - R\cos(\theta_{max} - \theta)$$ (6)

And the area distribution is defined as:

$$R = R_t + (R_e - R_t)\left[3\left(\frac{\theta}{\theta_{max}}\right)^2 - 2\left(\frac{\theta}{\theta_{max}}\right)^3\right]$$ (7)

Table 1 summarizes the parameters and which style of duct used in previous research on S-ducts.

Table 1. Parameters used in previous research on S-ducts

Research Group	L/D_e	A_t/A_e	Z_{offset}/D_e	Type
AGARD	3.0	1.4	0.9	M2129
DERA	3.0	1.4	0.9	M2129
Wellborn	4.1	1.5	1.09	Vakili
Whitelaw	3.0	1.4	0.9	Vakili
Reichert	3.0	1.4	0.9	Vakili
Anderson	2.5	1.4	0.9	M2129

The work performed by these groups has used a combination of wall static pressure taps, rakes across various stations down the duct's length, various 3- and 5-hole pressure probes, and laser-doppler velocimeter, [?], [?], [?], [?], [?] and [?]. Work has also been done by traversing 5-hole pressure probes across ducts at various stations. The wall

taps were positioned in both the axial and circumferential directions. The rakes had varying number of Pitot tubes to measure total pressure at each station.

From these measurements, they were able to show the static pressure gradients down the duct for the flow field, but not in as much detail that is necessary to begin attempting to predict behavior of the downstream flow field from upstream measurements. The flow behavior at various stations across the cross-section of the duct has been well-described by the various rakes and yaw meters used.

3. Flow Field Measurement Techniques

This chapter describes the flow field measurement techniques used for the experiments. Pressure-sensitive paint was used to obtain the wall static pressures, and a seven-hole pressure probe was used to measure the total and static pressures as well as the velocity vectors at the duct exit. This includes details on the theory, calibration, data collection and reduction and typical setups for each technique.

1. Pressure-Sensitive Paint

The use of pressure-sensitive paints (PSP) as a pressure measurement system has several advantages over traditional measurement systems. Paints are cheaper, easier to implement, provide better spatial resolution and non-intrusive to the flow. The development of PSP took place in the late 1980's at the Central Aero-Hydrodynamic Institute (TsAGI), Russia and at the University of Washington, USA in independent efforts, Guille [?] and Sakaue [?]. The use of PSP has grown significantly over the years and is used in the aerospace industry, university research, motorsport aerodynamic development, as well as many other areas.

PSP utilizes fluorescent/phosphorescent molecules as pressure sensors. The luminescence of the molecule changes in proportion to the partial pressure of oxygen in the test gas. The partial pressure of the oxygen can be related to static pressure and, hence, relate the luminescence to the static pressure. Generally, the sensor molecule is mixed in a binder that attaches it to the test surface. The luminescent molecule is referred to as a luminophore.

An optical system, such as a charge-coupled display (CCD) camera, measures these luminescent changes and will yield a full field pressure mapping. PSP is normally sprayed onto a model and is significantly less expensive than an array of pressure taps to produce an equivalent pressure mapping.

1. Measurement System

A PSP measurement system is comprised of two components, the pressure sensitive paint (PSP) and the measurement system. Figure 6 shows a typical PSP measurement system. The PSP provides the luminescent signal, where the light source, data acquisition hardware, and the data reduction programs comprise the measurement system.
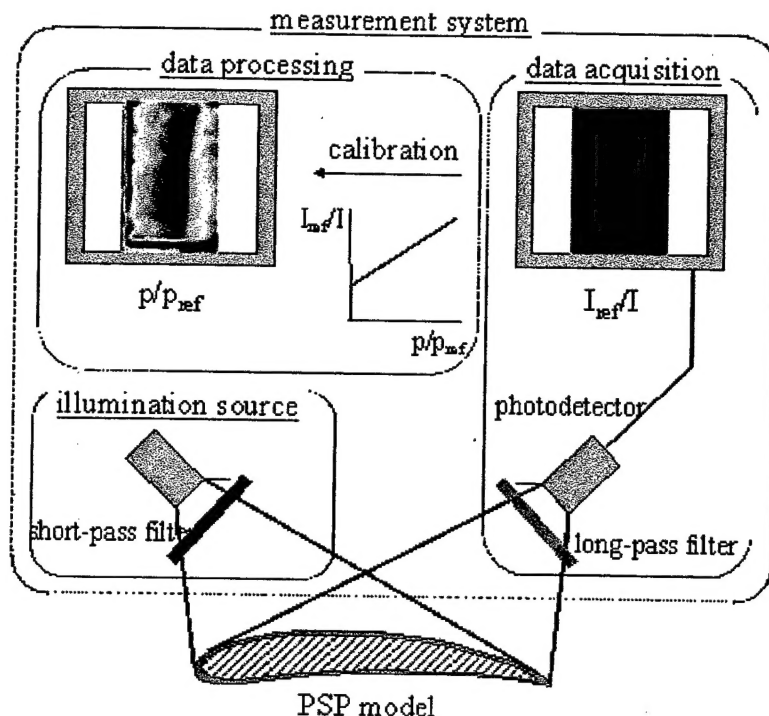
Figure 6. PSP Measurement System Schematic

The light source, such as a white lamp with a low-pass filter, a laser, or an light-emitting diode (LED), provides the appropriate wavelength light to the selected luminophore. In response, the molecule will emit a different wavelength signal as shown in Figure 7. This signal is measured by using a point photodetector such as a photo-multiplier tube (PMT) and photodiode or a CCD camera. The photodetector normally has an appropriate high-pass filter attached to it to remove the excitation wavelength from the signal. Either device measures the intensity level of the luminescent signal as an image. The data reduction scheme takes the signal and converts it into a pressure map using image registration and the appropriate calibration.
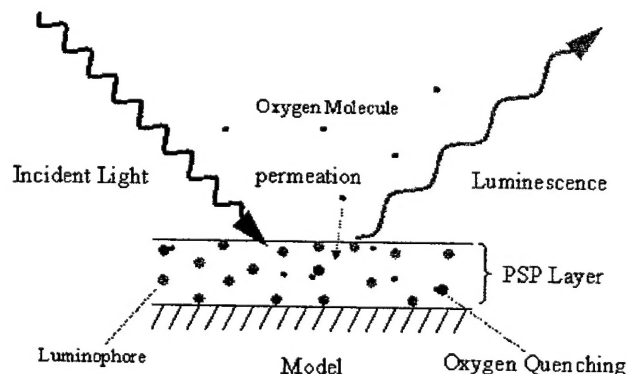
Figure 7. Typical activation and emission for a porous PSP

For a porous PSP similar to what will be used in this experiment, Figure 7 shows the permeation of the oxygen into the binder, the excitation of the luminophore by the light source and the emitted signal.

2. Data Reduction

As the pressure is increased, the oxygen molecules will permeate through the binder and quench the luminescence (oxygen quenching). From the change in luminescent intensity, the relationship between the change in surface pressures and the oxygen quenching can be determined. This relation is described by the Stern-Volmer equation,

$$\frac{I_o}{I} = \frac{\tau_o}{\tau} = 1 + k_q \tau_o \left[O_2 \right]$$ (8)

where I is the luminescent intensity, τ is the luminescent lifetime, k_q is the rate constant of quenching, and $\left[O_2 \right]$ is the concentration of oxygen. The subscript o denotes the absence of oxygen.

Henry's Law states that the oxygen concentration is proportional to the oxygen pressure which is proportional to the static pressure from the ideal gas law,

$$[O_2] \propto p_{O_2} \propto p$$ (9)

By substituting, Equation 9 into Equation 8 the Stern-Volmer equation becomes,

$$\frac{I_o}{I} = \frac{\tau_o}{\tau} = 1 + Kp$$ (10)

where K is the Stern-Volmer constant.

For intensity-based data acquisition, a reference (wind-off) image is required to properly calibrate the system. This calibration is necessary due to the fact the mixing of the luminophore in the binder, the spraying (application) of the paint, and the illumination of the light source is not uniform. If a ratio is taken in regards to the reference condition, the Stern-Volmer equation becomes,

$$\frac{I_{ref}}{I} = \frac{\tau_{ref}}{\tau} = A + B \frac{p}{p_{ref}}$$ (11)

where A and B are coefficients determined during the calibration process.

A rigorous derivation of this relation is performed by Sakaue in his Master's thesis, Sakaue [?].

3. Bathophen Ruthenium Chloride

The paint selected for this experiment is composed of Bathophen Ruthenium Chloride (BRC) as the luminophore and GE RTV 118 as the porous binder. This particular combination was selected due to its ease to make, durability and good response. The recipe and notes for making BRC in RTV 118 is in Appendix 5.

The excitation wavelength for the BRC luminophore is approximately 460nm and it emits around a peak of approximately 600nm as shown in Figure 9. The molecular structure is shown in Figure 8.
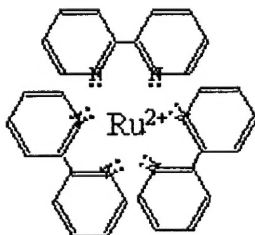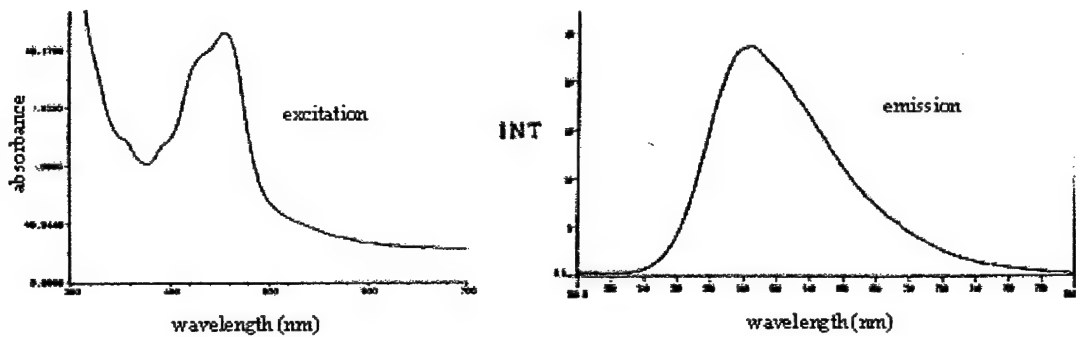
Figure 9. Excitation and emission spectrums for Bathophen Ruthenium Chloride

4. PSP Calibration

An *a priori* calibration was performed on each paint mixture used in this experiment. When the test model was painted, a calibration sample was also made from the same material as the test model. This sample was placed into a calibration chamber where the pressure can be varied from atmospheric down to vacuum.

To calibrate a given paint, the chamber was dropped to near vacuum, normally less than 0.1 psia, where a reference image was taken. Then the pressure was increased by approximately 1.0 psia steps with images and pressure readings being taken at each step. The images would then be brought into Matlab where the intensity ratios were determined for each image based off of the reference image. The Stern-Volmer equation was used to generate the pressure ratios from these intensity ratios. Figure 10 shows the calibration curve fits for each paint mixture used.
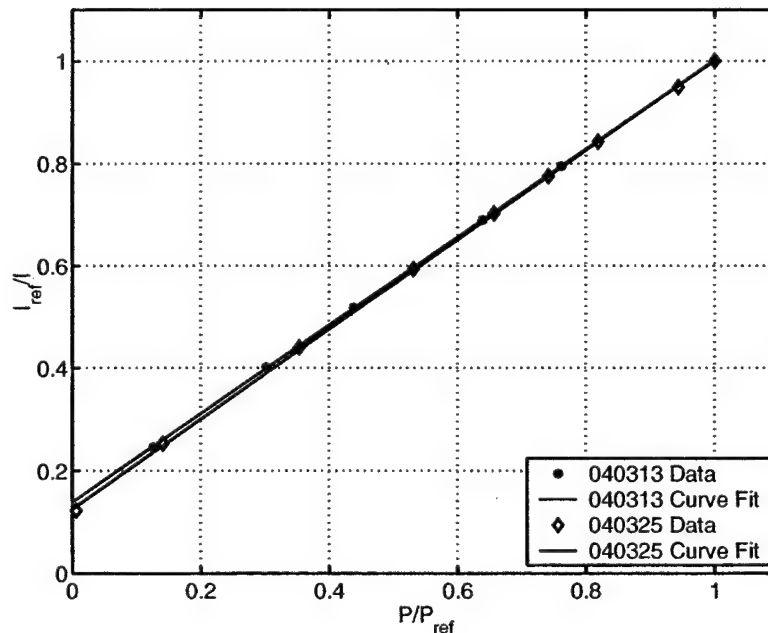
Figure 10. Curve Fits for PSP Calibration

5. PSP Data Reduction

A similar technique was used for the experimental data reduction. A reference image was taken prior to starting the wind tunnel. At each mach number during the run, a series of five images was recorded.

Due to model movement during testing, each image needs to be aligned to the reference image using the reference markers on the duct. This correction is critical to getting accurate data from the images. Even small misalignments by one or two pixels can dramatically shift results. Image registration and alignment was performed using a program called AFIX. AFIX is a program developed by Yves Le Sant for the ONERA-DAFE wind tunnel in France.

Once the image alignment has been completed, Matlab again was used to generate the intensity ratios and, via Stern-Volmer, the pressure map of the duct. Once the pressure map is computed, then the data can be extracted from regions of interest.

2. Seven-Hole Pressure Probe

Multi-hole pressure probes can be used to measure flow angles as well as total and static pressures. The concept is that a flow field with a given velocity, static pressure and flow angle will generate a unique set of pressure measurements for the array of holes on the probe.

The seven-hole probe originated at the U.S. Air Force Academy through work by Gallington, Gallington [?]. The goal of the seven-hole probe was to provide details on the flow field where other multi-hole probes failed. It has been used in automotive wind tunnel testing, wall strut interactions, and in studying vortex formations on various bodies, Sumner [?].
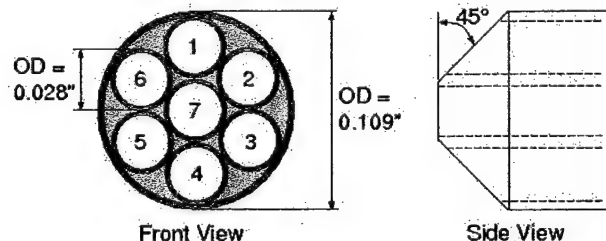
Figure 11. Front and side view of seven-hole probe and port numbering scheme

The probe measures seven unique pressures that are used to compute the total and static pressures as well as the flow angles, pitch and yaw, of the flow field as shown in Figure 12. This leads to an over determined system since there are seven measured values to calculate four flow properties.
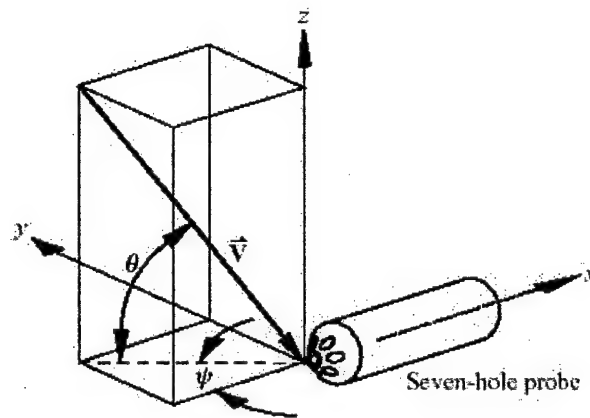
Figure 12. Coordinate system for seven-hole probe measurements, Sumner [?]

At low flow angles, flow remains attached over the entire surface of the probe, and the central port reads the highest pressure. Pressure information from all seven holes will be used to determine the flow conditions. At high flow angles, as shown in Figure 13, it is possible for the flow around the tip of the probe to separate. When this occurs a port other than the center port will read the highest pressure, and, subsequently, a subset of the pressure data will be used to calculate the flow field properties. This technique has been shown to extend the usable range of the probe, Zilliac [??0].
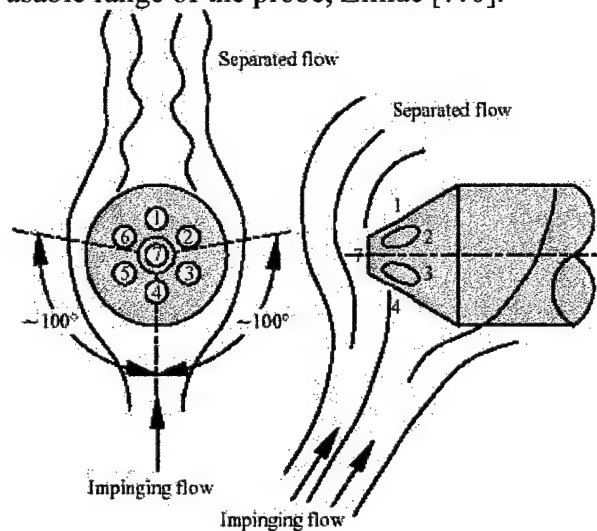
Figure 13. Flow around tip of seven-hole probe, Sumner [?]

The construction of a seven-hole probe is simpler than other multi-hole probes. An array of six tubes can be placed around a center tube all of equal diameter within an outside tube of three-times the inner tubes' diameter, as shown in Figure 11. The seven-hole probe used was constructed of seven stainless steel tubes of equal diameter inserted into a larger diameter steel tube with the end chamfered at a 45 degree half-angle cone, see Figure 11. The probe has an outer diameter of 0.109 inches with each inner tube having

an outer diameter of 0.35 and is approximately 5 inches long. The probe is illustrated in Figure 14.
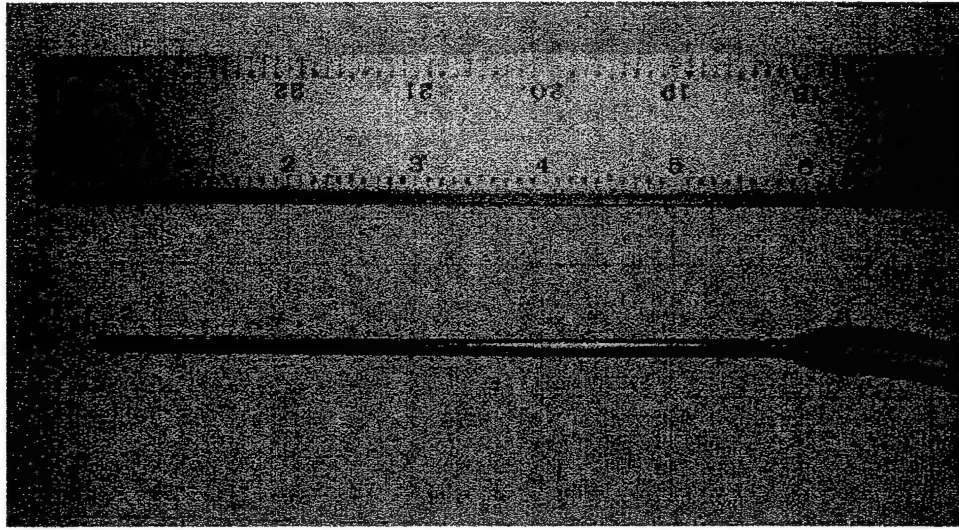
Figure 14. Image of seven-hole probe used in work by Lindqvist [?]

1. Probe Calibration

In order to be able to produce useful data from a seven-hole probe, it must be calibrated in a known flow field. This establishes the relationship between the pressure values measured by the probe and known flow field values, pitch, yaw, static pressure and total pressure, at each calibration point.

As with previous work by Lindqvist [?] and Campbell [?], the calibration procedure was used from Zilliac [??0]. Zilliac's work developed a non-nulling calibration method for a large range of flow angles. In this method, a set of non-dimensional coefficients determined from the seven pressure measurements at each port, $p1, p2, ..., p7$ and is correlated to the known properties in the flow field during measurement.

Since it is possible for the some of the pressure ports to be in a separated flow region and because of that produce erroneous measurements, part of Zilliac's method involves a sectoring scheme which determines the sector and, thereby, the equations to be used based on the which port has the highest pressure measurement. This sectoring scheme increases the sensitivity and accuracy of the probe by eliminating ports that are in the separated flow region.

The calibration method used in this experiment was generated by Lindqvist [?]. Details as to this calibration can be found in Lindqvist's thesis [?]. The calibration range for the pitch and yaw was from -44 degrees to +44 degrees in 4 degree increments. At each data point, 20 samples were taken and averaged. This produces 529 data points for the calibration. Figure 15 shows the mapping of the highest port pressure at each calibration point. This mapping is then used to determine which set of equations is to be used to determine the non-dimensional coefficients.
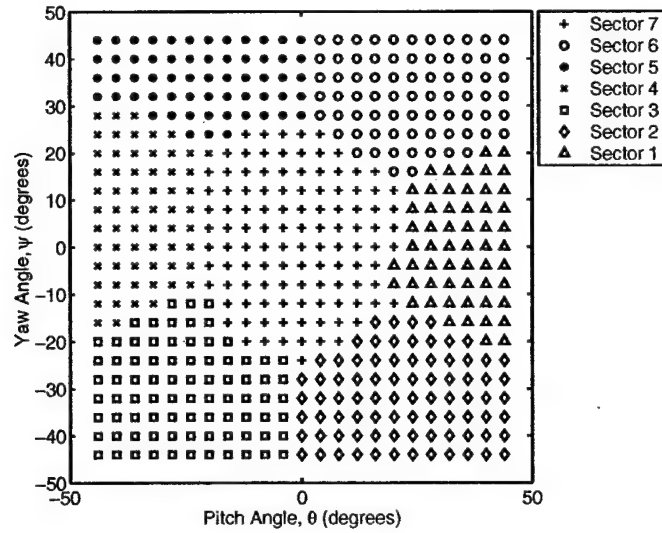
Figure 15. Port mapping showing port with highest pressure readings for calibration data

2. Probe Calibration Equations

For low flow angles, sector 7 is the highest pressure value. From Zilliac, the following definitions are used to determine the non-dimensional pressure coefficients. The pitch pressure coefficient C_θ and yaw pressure coefficient C_ψ are defined as,

$$C_\theta = C_{Pa} + \frac{C_{Pb} - C_{Pc}}{2} \quad \text{and} \quad C_\psi = \frac{1}{\sqrt{3}}\left(C_{Pb} + C_{Pc}\right) \tag{12}$$

where the non-dimensional coefficients C_{Pa}, C_{Pb}, and C_{Pc} are defined as,

$$C_{Pa} = \frac{p_4 - p_1}{p_7 - \bar{p}}, C_{Pb} = \frac{p_3 - p_6}{p_7 - \bar{p}} \quad \text{and} \quad C_{Pc} = \frac{p_2 - p_5}{p_7 - \bar{p}}. \tag{13}$$

$\bar{p}$ is the arithmetic mean of the outer pressure ports,

$$\bar{p} = \frac{1}{6}\sum_{i=1}^{6} p_i \tag{14}$$

The non-dimensional coefficients for total pressure C_{Ptot} and static pressure C_{Pstat} are defined as,

$$C_{Ptot} = \frac{p_7 - p_{total}}{p_7 - \bar{p}} \quad \text{and} \quad C_{Pstat} = \frac{\bar{p} - p_{static}}{p_7 - \bar{p}} \tag{15}$$

For higher flow angles, there is the possibility of separated flow over the probe tip. According to Schlicting, a cylinder in a turbulent flow has separation points over 100 degrees from the frontal stagnation point and for a conical body they will be even further away, Gerner et al. [?]. As shown in Figure 13, the result for a probe with separated flow over the tip is that at least three of the outer ports must always be in the attached flow.

Thus, for the sectoring scheme outlined by Zilliac, if the highest pressure port is not port 7, a subset of the pressure ports is used to calculate the non-dimensional coefficients for the calibration, Zilliac [??0].

The non-dimensional pitch and yaw pressure coefficients are defined by

$$C_{\theta,n} = \frac{p_n - p_7}{p_n - \left(p_{n-} + p_{n+}\right)/2} \tag{16}$$

$$C_{\psi,n} = \frac{p_{n-} - p_{n+}}{p_n - \left(p_{n-} + p_{n+}\right)/2} \tag{17}$$

where n is the port number with the highest pressure, $n-$ is the port one step counter-clockwise, and $n+$ is the port one step clockwise.

3. Probe Calibration Data

Since the probe used in the experiment was the same probe used by Lindqvist, the calibration data from that previous work was used for this experiment, Lindqvist [?]. This section explains the implementation of differential pressures instead of absolute pressures for the generation of the non-dimensional pressure coefficients.

The definitions from Zilliac have the pressure measurements defined as absolute pressure values. The pressure scanner used measures in differential pressure based off of a common reference pressure p_{ref}. The relationship between the differential pressure and the reference pressure is defined as,

$$p_i^* = p_i - p_{ref} \tag{18}$$

where the reference pressure is set to the freestream static pressure p_∞.

The use of differential pressures instead of absolute pressures does not change the result of the calibration procedure. By substituting equation 18 into equations 12, 13, 14 and 15, the equations are converted from being based on absolute pressures to differential pressures.

An example is shown by performing this operation on equation 13 for the C_{Pa} equation,

$$C_{pa} = \frac{p_4 - p_1}{p_7 - \bar{p}} = \frac{(p_4 - p_{ref}) - (p_1 - p_{ref})}{(p_7 - p_{ref}) - (\bar{p} - p_{ref})} = \frac{p_4^* - p_1^*}{p_7^* - \bar{p}^*} \tag{19}$$

From the differential pressures, all four non-dimensional coefficients can be calculated. The relationships for $\theta(C_\theta, C_\psi)$, $\psi(C_\theta, C_\psi)$, $C_{Ptot}(C_\theta, C_\psi)$, and $C_{Pstat}(C_\theta, C_\psi)$ are displayed in the following graphs for sector 7. The graphs for the other 6 sectors are shown in Appendix ?.
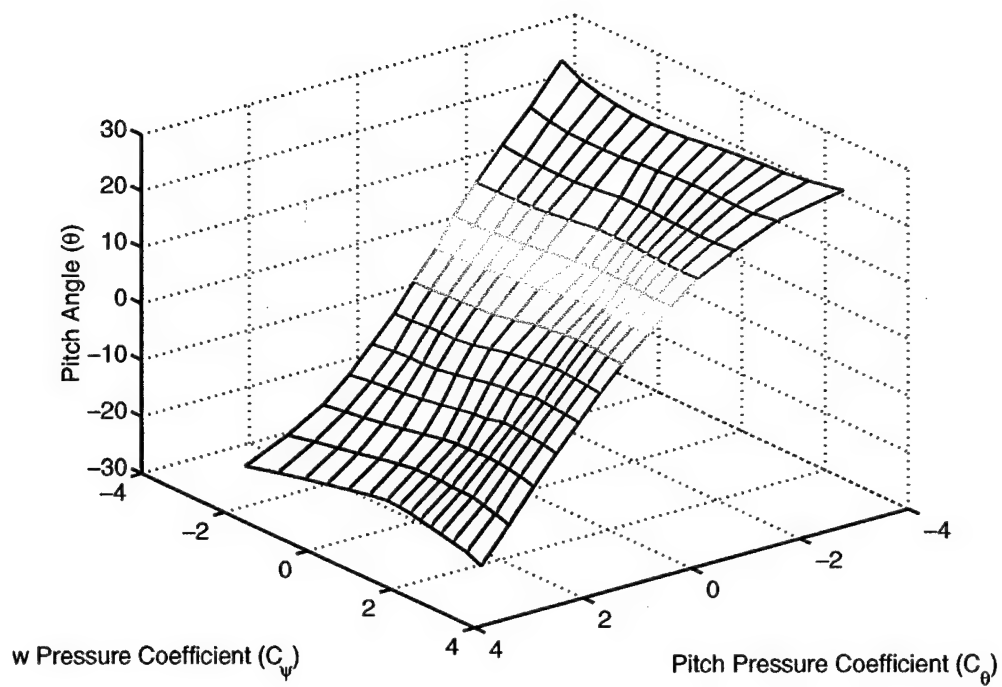
(a) $\theta(C_\theta, C_\psi)$
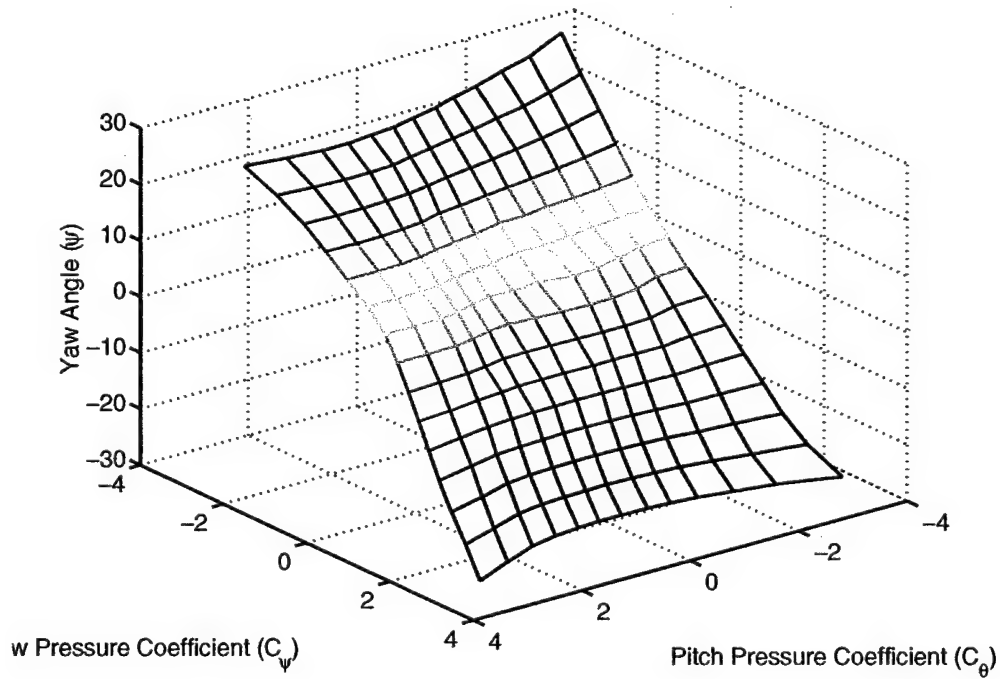
(b) $\psi(C_\theta, C_\psi)$

Figure 16. Calibration data for Sector 7 for a seven-hole pressure probe
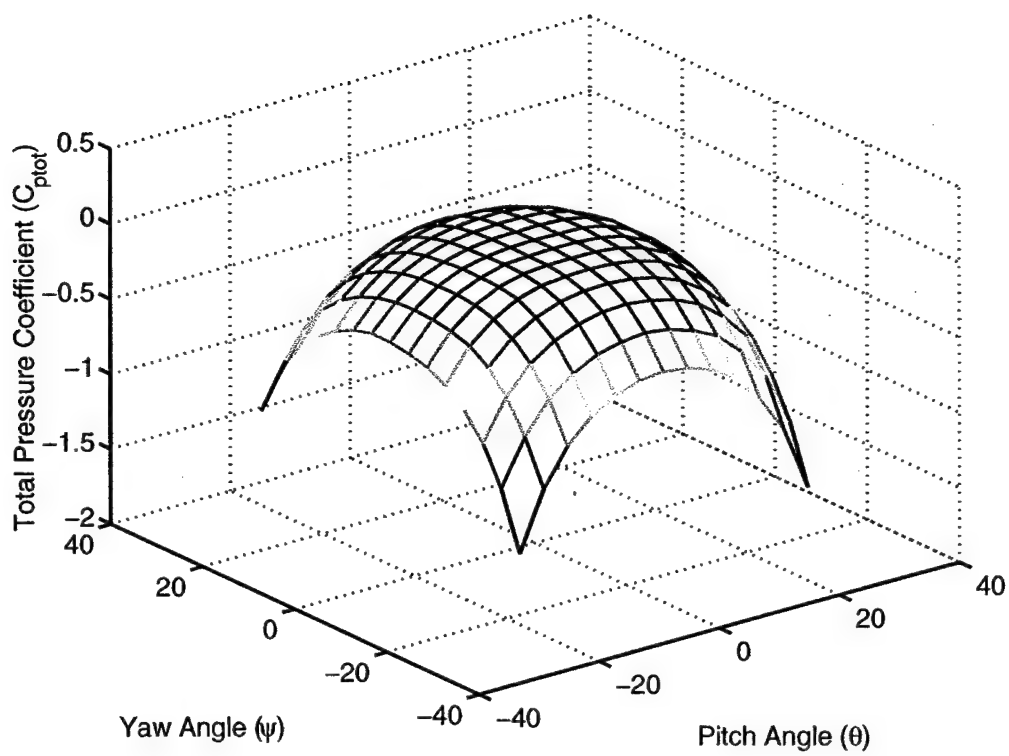
(a) $C_{Ptot}(\theta, \psi)$
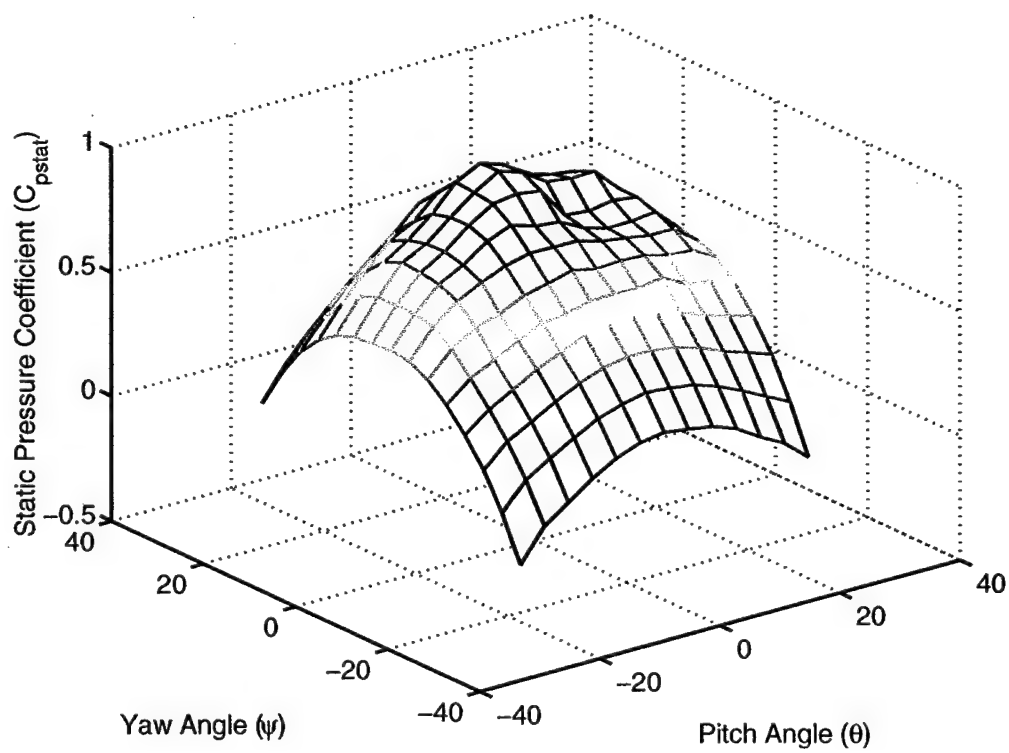
(b) $C_{Pstat}(\theta, \psi)$

Figure 17. Calibration data for Sector 7 for a seven-hole pressure probe

4. Probe Data Reduction

To determine properties in an unknown flow field, the reverse procedure of the calibration method is used. The seven measured differential pressures from the probe are known, whereas the flow angles and total and static pressures are not.

The seven measured pressures are used to calculate the pitch pressure coefficient C_θ and the yaw pressure coefficient C_ψ. A check needs to be performed to determine which port has the highest pressure. This dictates which of the seven sector equation sets to be used in calculating C_θ and C_ψ. Once this is selected, C_θ and C_ψ are calculated and the pitch θ and yaw ψ values are found through linear interpolation of the calibration data presented above.

$$\theta = \theta(C_\theta, C_\psi) \tag{20}$$

$$\psi = \psi(C_\theta, C_\psi). \tag{21}$$

The total and static pressure coefficients are found by the same method using the values for pitch and yaw and the calibration data figure 16 and 17,

$$C_{Ptot} = C_{Ptot}(\theta, \psi) \tag{22}$$

$$C_{Pstat} = C_{Pstat}(\theta, \psi). \tag{23}$$

The total and static pressures are determined from

$$p_{tot} = p_7 - (p_7 - \overline{p})C_{Ptot} \tag{24}$$

$$p_{stat} = \overline{p} - (p_7 - \overline{p})C_{Pstat}. \tag{25}$$

The magnitude of the flow velocity is calculated by

$$V = \sqrt{\frac{2}{\rho}(p_7 - \overline{p})(1 + C_{Pstat} - C_{Ptot})} \tag{26}$$

where the Cartesian velocity components are decomposed by

$$u = V\cos(\theta)\cos(\psi) \tag{27}$$
$$v = -V\sin(\theta) \tag{28}$$
$$z = V\cos(\theta)\sin(\psi) \tag{29}$$

according to the coordinate system detailed in Figure 12.

The equations above are all show for absolute pressures, but there is no effect by using differential pressures in the data reduction process.

4. Experimental Setup

The test rig for these experiments will be based on the transonic tunnel at Purdue University's Aerospace Laboratories. The transonic tunnel is a Chicago Blower, Model 2T-30-28, which is a centrifugal blower. The blower has a flow rate of 2950 CFM. A diffuser is attached to the blower's inlet with a honeycomb mesh to help prevent blade noise from transmitting upstream. A transonic test section is normally mounted to the diffuser with a wide-mouth inlet. For the purposes of these experiments, the test section was not required so an adapter was built to mount the various ducts to the transonic tunnel. Figure 18 and 19 show the configurations used for both the PSP and seven-hole probe setups.
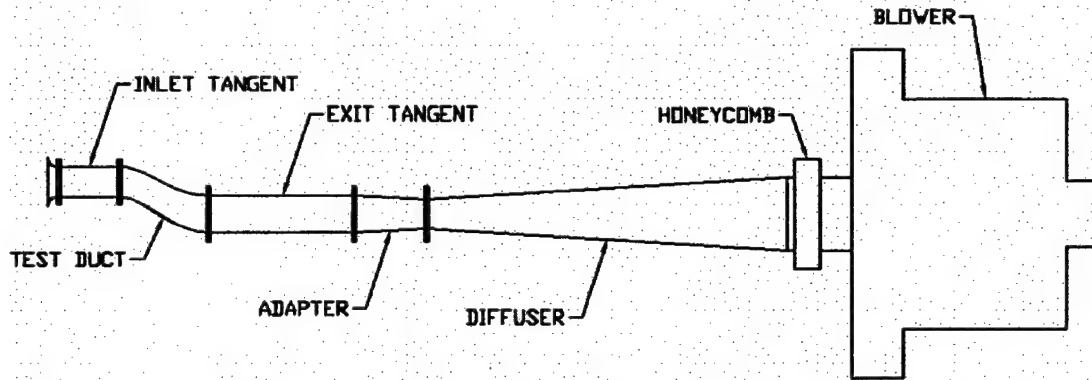
Figure 18. Test rig schematic with PSP configuration
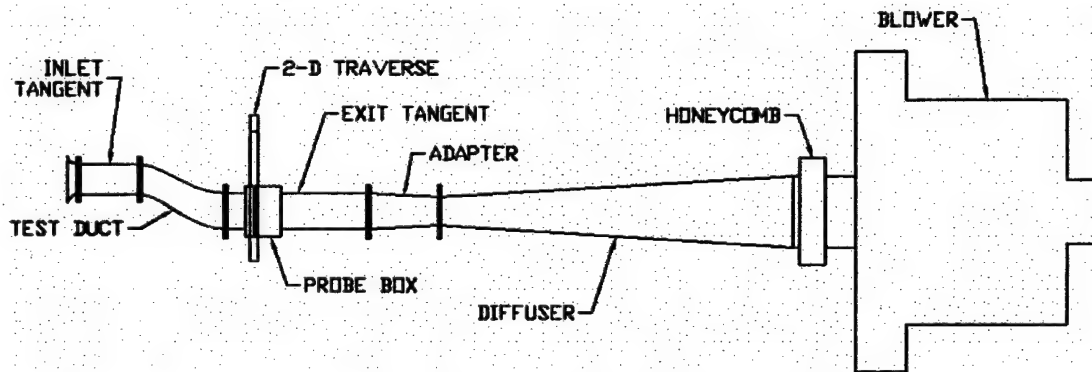
Figure 19. Test rig schematic with seven-hole probe configuration

Figure 20. Image of test rig with seven-hole probe configuration

In order to help isolate the test ducts from possible upstream noise, an exit tangent is mounted to the duct exit. The length of the tangent is four times the engine face diameter. Inlet tangents set the boundary layer size at the entrance of the duct. Two lengths are used in these experiments. The first is of one inlet diameter length, and the other is of two inlet diameter length.

This test rig was capable of mach numbers from Mach 0.20 to 0.90 depending on the configuration in use.

1. Duct Geometry

Based off of previous work by the by AGARD FDP working group, Anderson [?] and the abundance of data both through CFD and experimental studies, the M2129 duct was selected for this study. Table 2 shows the geometric parameters used to construct the test ducts.

Table 2. Geometric Parameters for Test Ducts

Name	L/D_e	A_i/A_e	Z_{offset}/D_e	Type
M2129L	3.2	1.4	0.9	M2129
M2129S	2.5	1.4	0.9	M2129
Semi-Circle	2.5	1.5	0.5	M2129

The M2129L duct is the validation case for the test setup as it closely matches the parameters used in previous research as shown in Table 1. A comparison of the centerline geometries is shown in Figure 21.
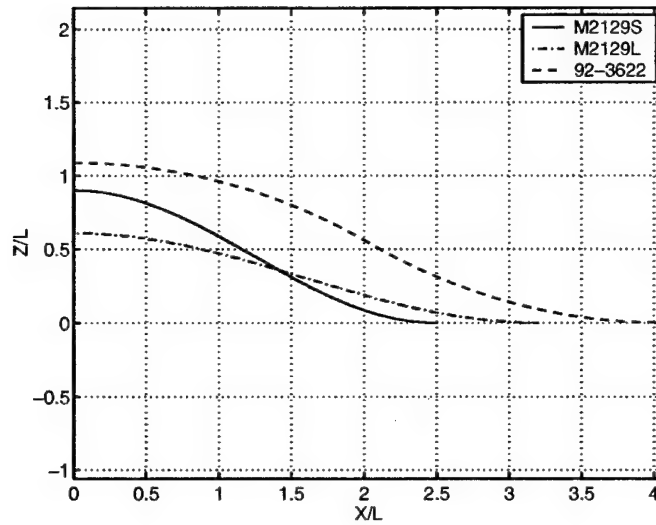
Figure 21. Geometry Comparison of M2129L, M2129S, and a Vakili-style duct, [?]

The semi-circle duct is based on the M2129 geometry. It has the M2129 upper surface and centerline combined with a lower surface that goes from a flat to a full circle to create the semi-circle inlet shape. The arc length of the lower surface is controlled by equation 30.

$$\theta_{lower} = \text{offset} + (\pi - \text{offset})\left[1 + 3\left(1 - \frac{x_{cl}}{L}\right)^4 - 4\left(1 - \frac{x_{cl}}{L}\right)^3\right] \tag{30}$$

where *offset* is a small value increment to prevent the lower arc length from being zero length.

Figure 22 shows the geometry for each of the ducts tested.
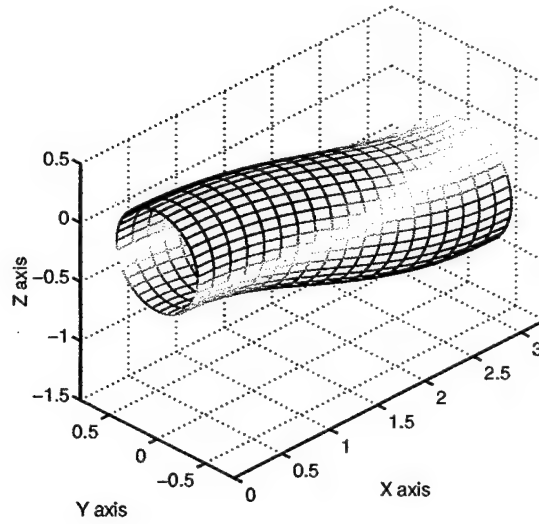
(a) M2129L Geometry
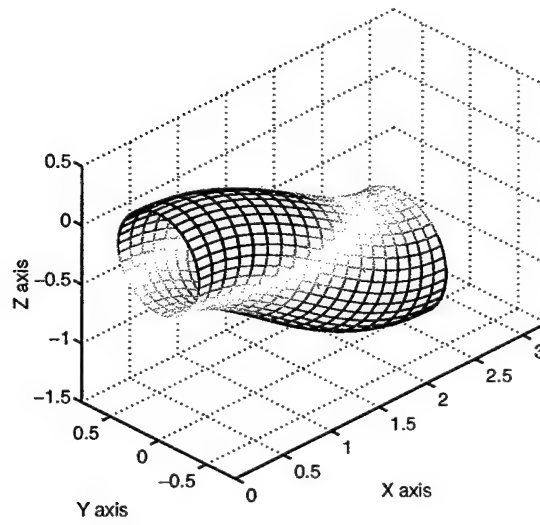
(b) M2129S Geometry
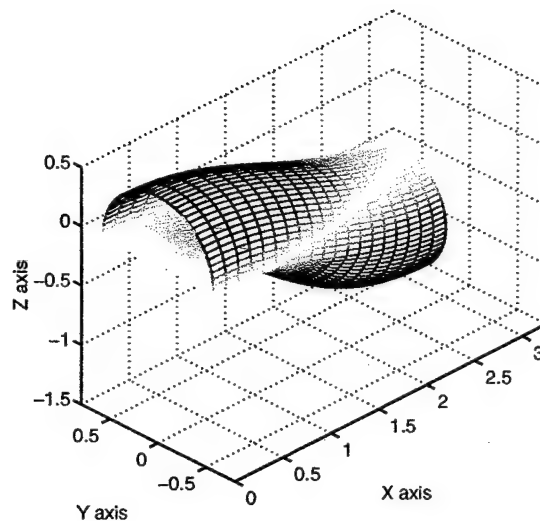
(c) Semicircle Geometry

Figure 22. Calibration data for Sector 7 for a seven-hole pressure probe

A pressure tap was placed in the inlet tangents to set the Mach number of the flow.
For each data run, the following procedure was used. After startup, the velocity of the tunnel was set and allowed to run for 10 minutes to allow for any startup transients to damp out and for the motor warm up so that there would be no RPM fluctuations due to a change in motor temperature.

2. PSP

The data collection for the PSP data is shown below. An Innovative Scientific Solution Incorporated (ISSI) light source Model LM4 was used to illuminate the model. It was a 4 inch diameter light source that emitted a blue-wavelength (469 nm) light. A Photometrics Sensys 12-bit Charge-couple Display (CCD) camera with a image size of 768x512 pixels measured the intensity of the PSP signal. A 600 nm high-pass filter was affixed to the camera lens to remove the illumination source from the PSP signal. At each configuration and mach number, five images were taken and averaged to produce a data image.
A second pressure tap was added 0.5 inches inside the entrance of the duct to provide for correction of the PSP calibration.

3. Seven-hole Probe

For the seven-hole probe data acquisition, one change was made to the physical test setup. The exit tangents were modified to allow the insertion of the seven-hole probe into the flow field. A probe box was added to allow the probe the necessary volume to traverse the flow field, shown in Figure 23.
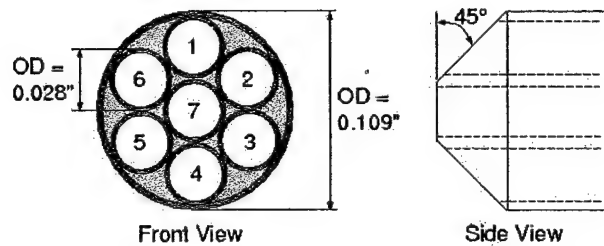
Figure 23. Image of Seven-Hole Probe Test Rig

Inserts were also added to the probe box to minimize any disturbances due to flow separation from the sharp changes in geometry at the junction of the probe box and tangent.

A 2-axis traverse was built using two Velmex Uni-Slides, Model MB2521W1J-S21/2, with a Velmex NF90 motor controller. The step motor on the slides had a step increment of 4000 steps per inch (0.00025 inches per step). A small strut was made to support the seven-hole probe in the flow field.

Each port of the probe was attached to a pressure scanner by Tygon tubing. Port i of the probe corresponds to the pressure reading p_i, where the numbering convention of the seven-hole pressure probe is depicted in Figure 11.

The pressure scanner used is a Pressure Systems Incorporated Model 3200. The 3200 model is comprised of 32 independent pressure transducers that measure differential pressures in the range of ±1 pounds per square inch (PSI). One side of each transducer was attached to a common reference pressure p_{ref}, which in this case was atmospheric pressure.
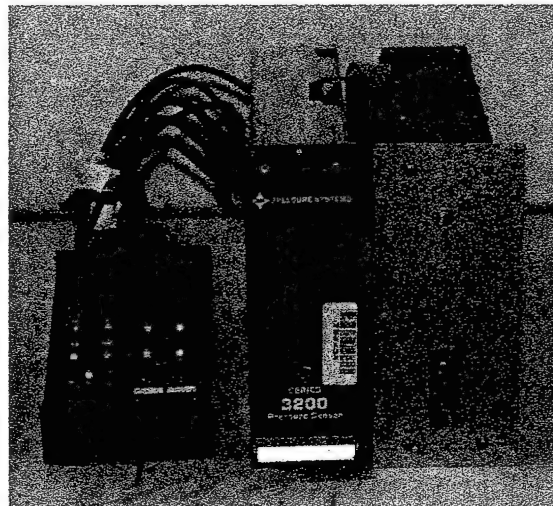
Figure 24. P3200 Pressure Scanner used with the seven-hole probe

The scanner originally communicated through a parallel port connection to a PC, but this has been previously removed. The current configuration has each pressure transducer wired directly at a National Instruments PCI-6025E data acquisition board using a BNC-2110 interface box.
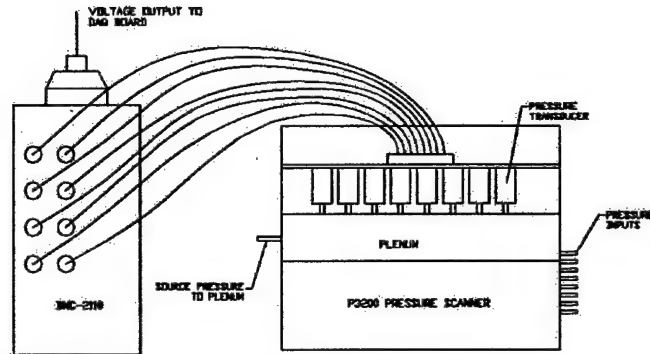
Figure 25. Wiring Schematic for P3200 Pressure Scanner

Each pressure transducer was independently calibrated by supplying a series of known pressures to the transducer and its corresponding voltage output. A linear curve fit for each transducer was then used to determine pressures from the measured voltages. See Appendix ? for more detail.

A LabView program was written to interface with both the motor controller and the pressure scanner. It worked by reading in a coordinate file of the survey grid and using that data to move the traverse through the flow field. At each point in the flow field, simultaneous pressure measurements consisted of at least a five second sample at 200 Hz to determine an average value for each port.

Due to symmetry in the flow field of the ducts, the survey grid only traversed half of the duct as shown in Figure 26.
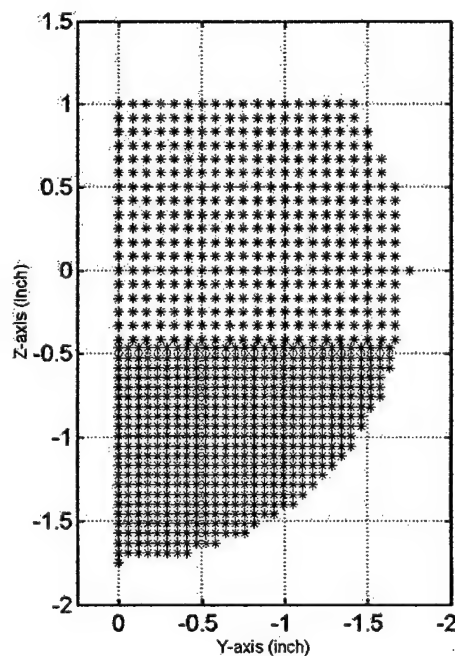
Figure 26. Sample grid used for seven-hole probe data collection

Also, shown is the variation in grid density across the engine face. A denser grid was used in the lower section of the duct to provide a better spatial resolution of the disturbed flow region. Also, the sample time in each region could be independently controlled to enable longer sample times in the lower region due to unsteadiness in the flow. This unsteadiness is address in more detail in Appendix F.

5. BRC in RTV 118 Recipe

The recipe for BRC in RTV118 paint is as follows:
- 4mg Bathophen Ruthenium Chloride
- 20mL Dichloro-Methane, CH_2Cl_2
- 2.5mL GE RTV 118
- 1.6g Silica gel

Dissolve the BRC in the dichloromethane. Then add the silica gel and stir until thoroughly mixed. Normally, this takes about five minutes of hand stirring. Then add the RTV and stir again until it is completely dissolved. This should take another 5-10 minutes of hand stirring.

It is advised to make small quantities as a time, since the solution does not stay liquid for an extended period of time. Normally within a few hours, the solution will have hardened nearly into a solid.

6. PSP Bulk Data

A. M2129L, Mach = 0.2-0.8
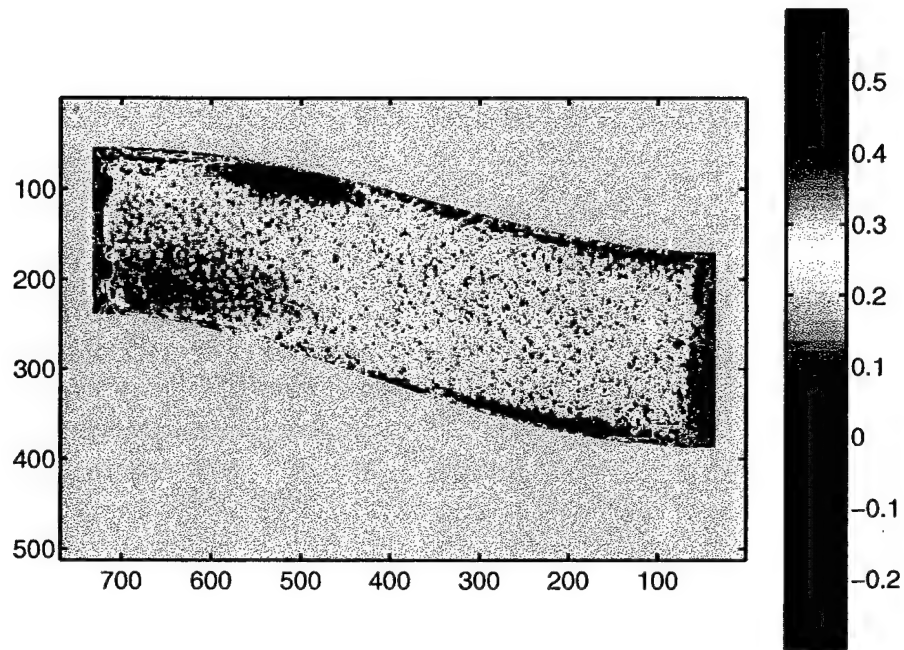
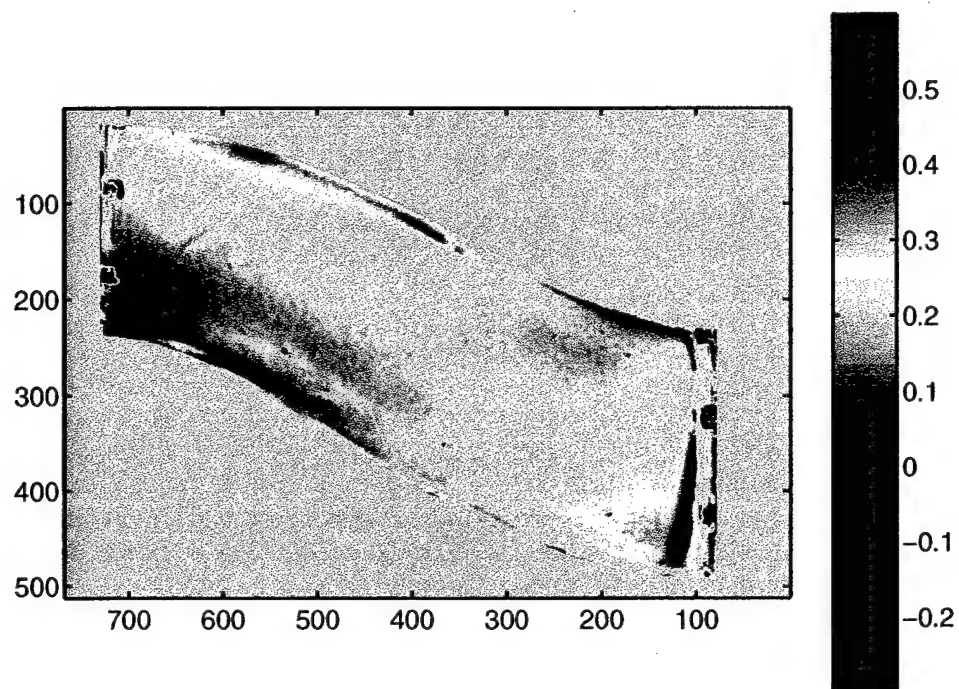Figure 27. C_P Mapping for M2129L with 1D Tangent at Mach = 0.2
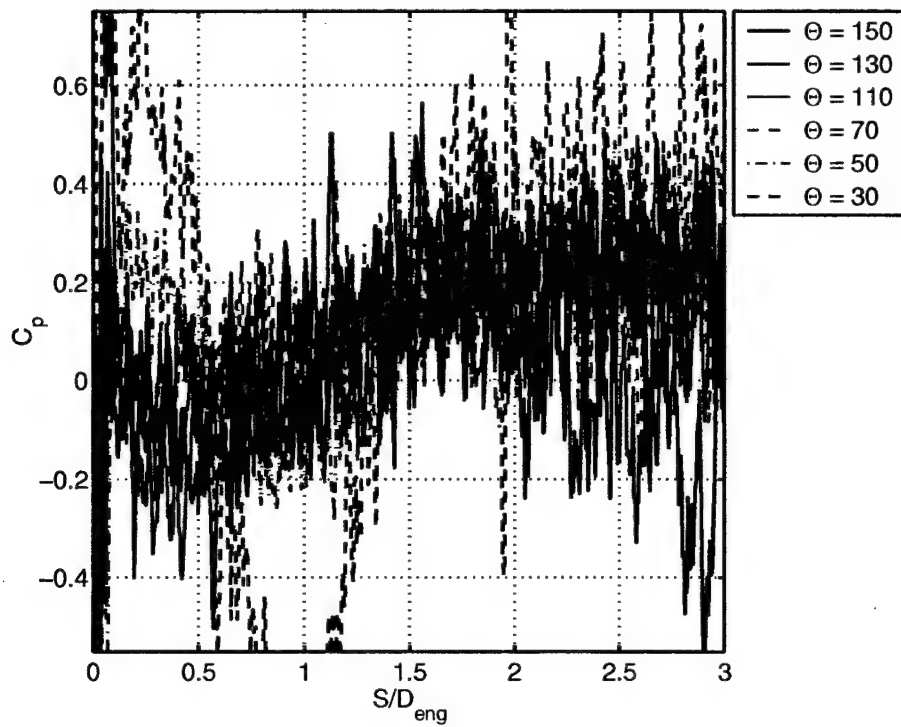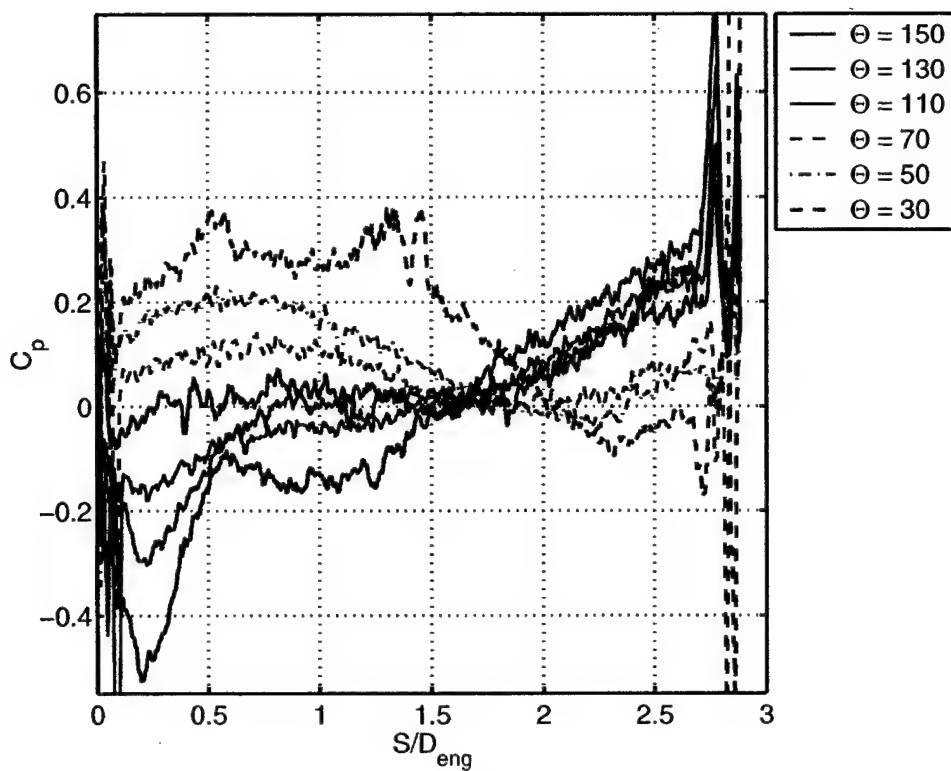
(a)Axial Distribution of Cp
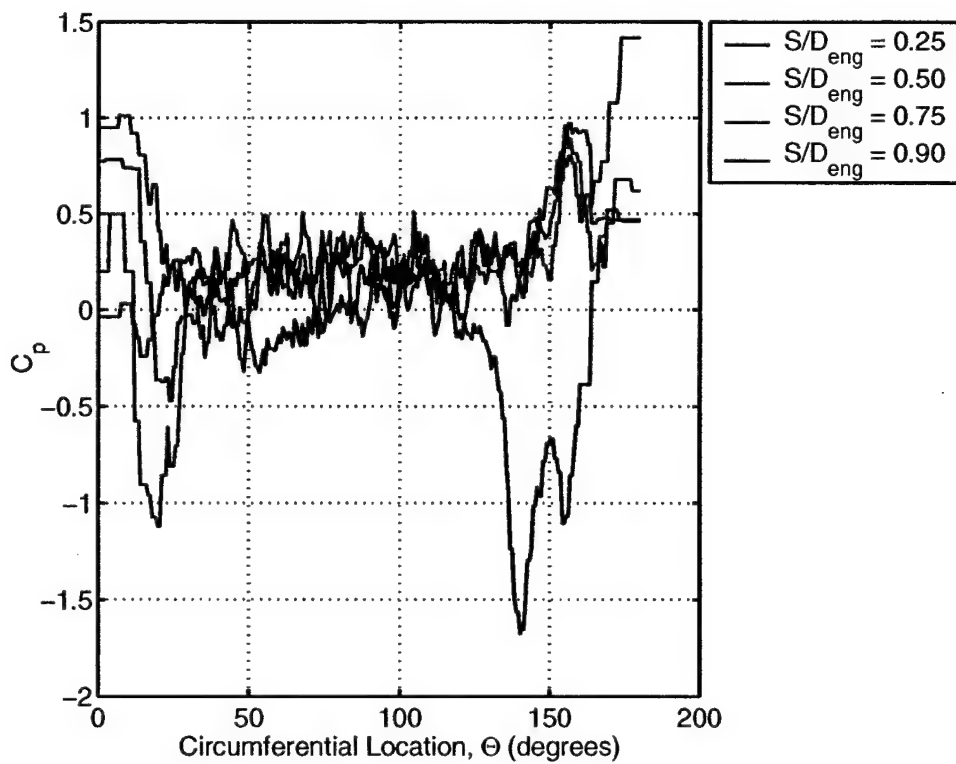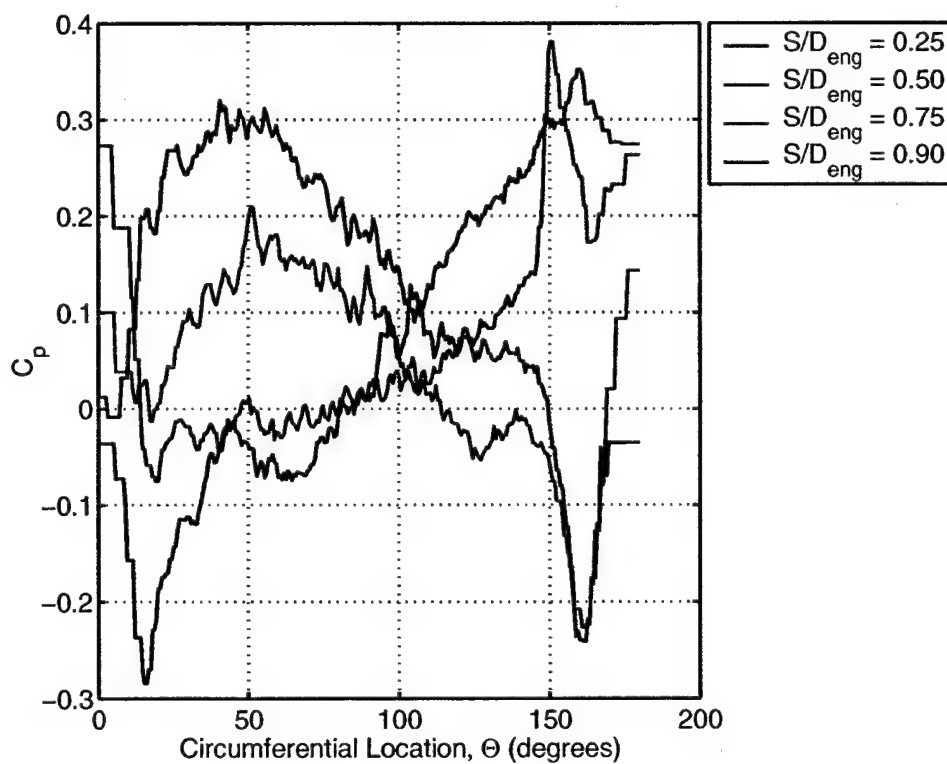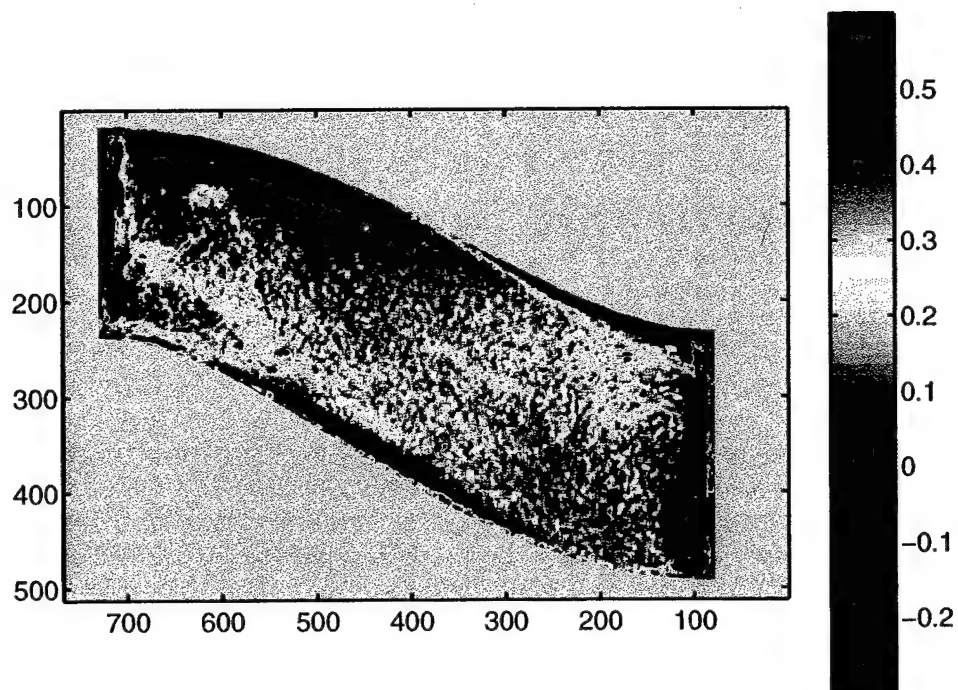

(b)Circumferential Distribution of Cp

Figure 28. PSP Data for M2129L with 1D Tangent at Mach = 0.2
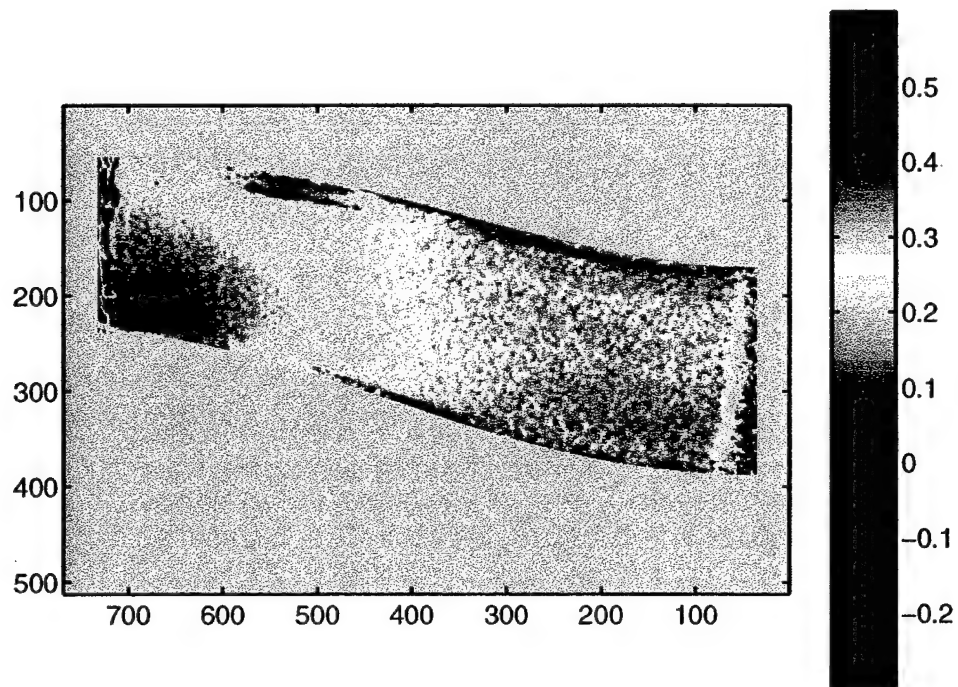
Figure 29. C_P **Mapping for M2129L with 1D Tangent at Mach = 0.4**
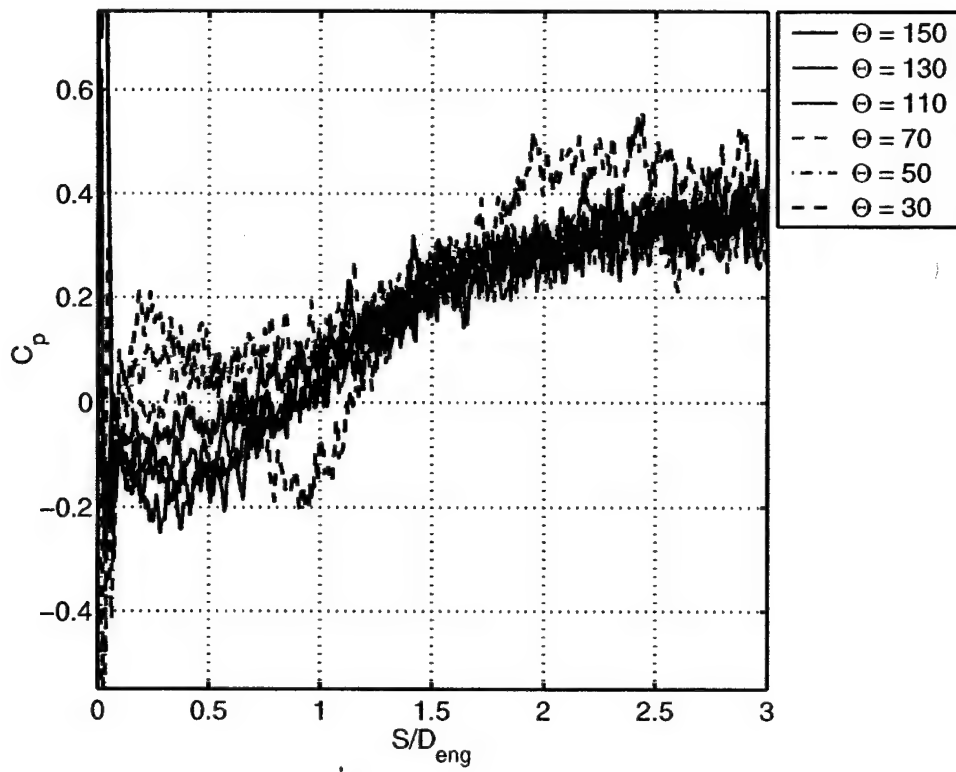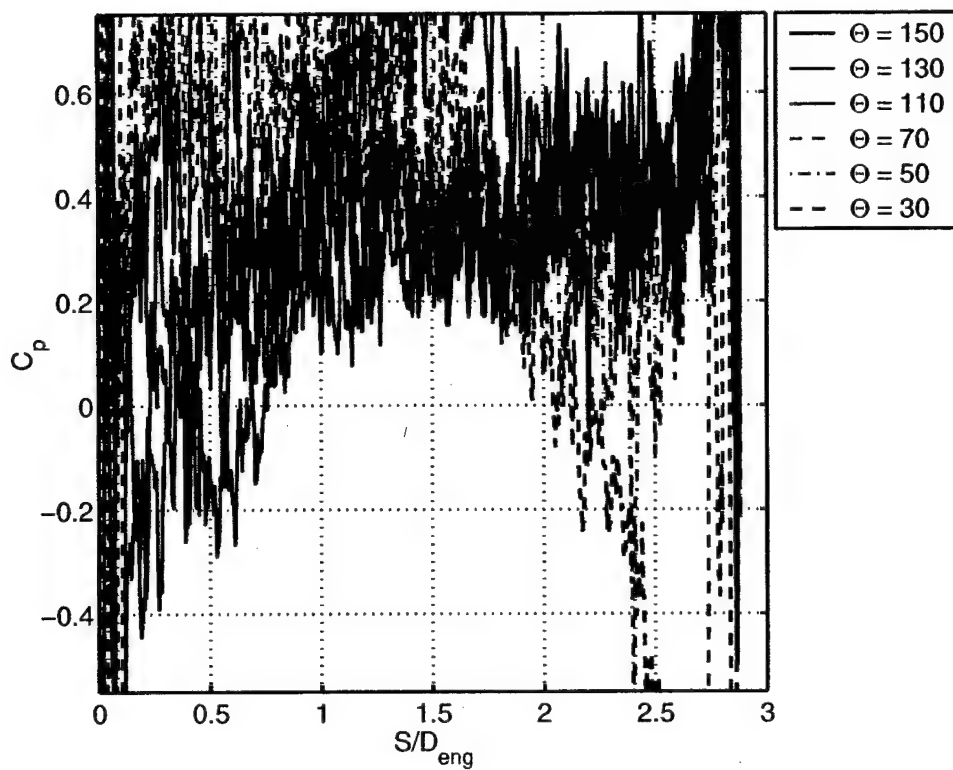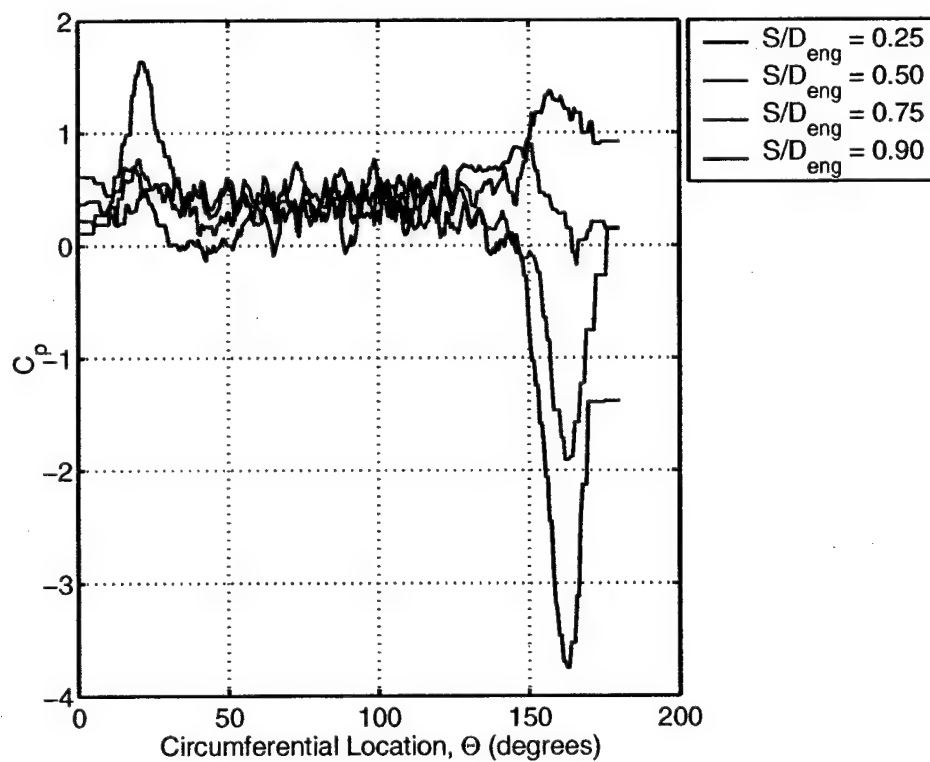
(a)Axial Distribution of Cp
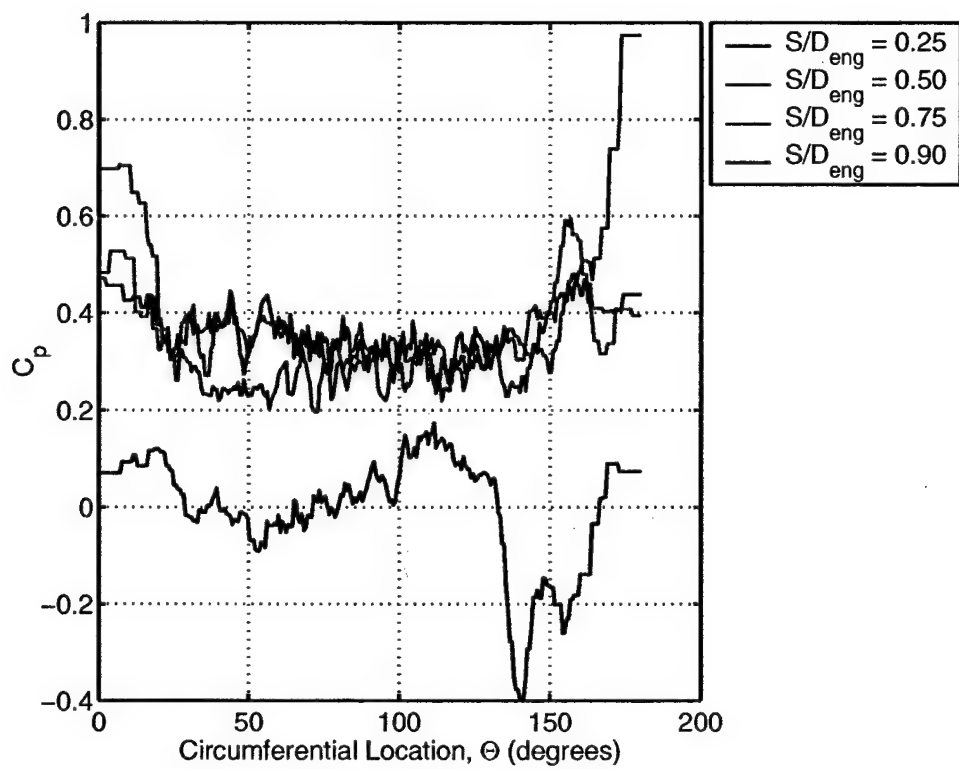
(a)Circumferential Distribution of Cp

Figure 30. PSP Data for M2129L with 1D Tangent at Mach = 0.4
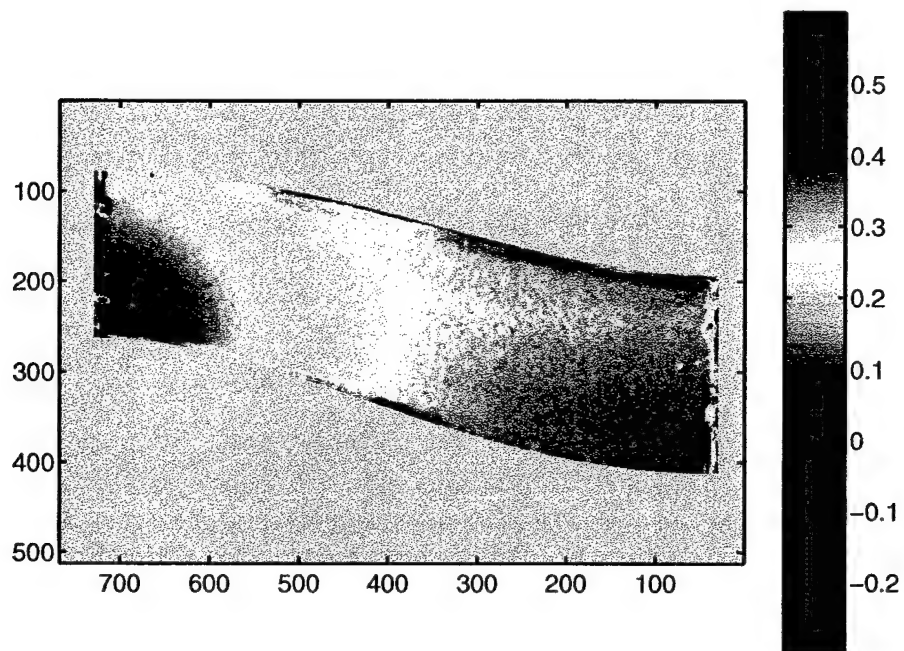
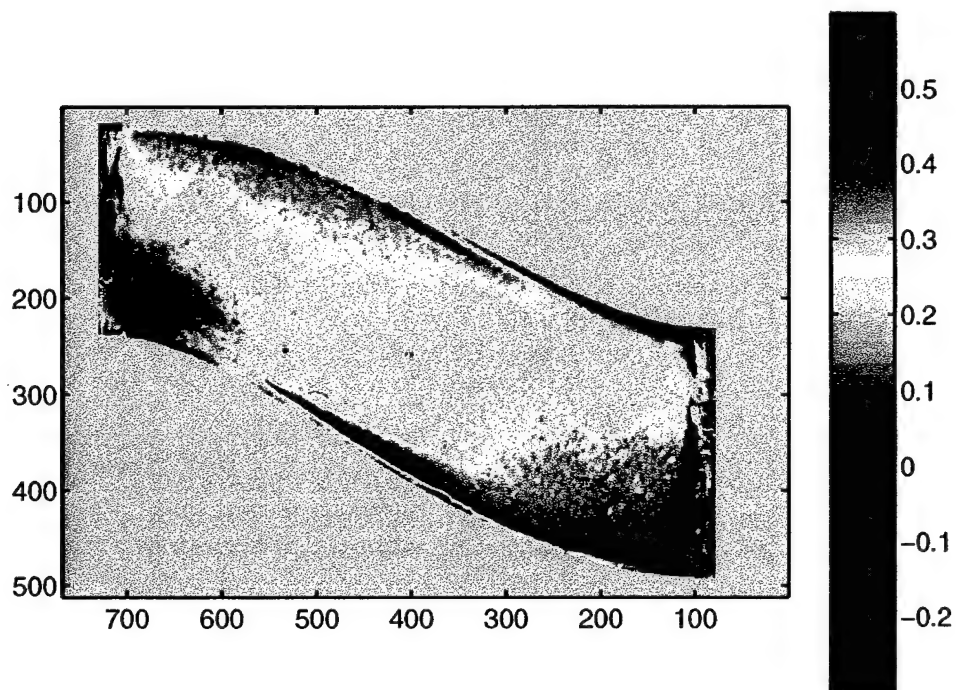**Figure 31. Mapping for M2129L with 1D Tangent at Mach = 0.6**
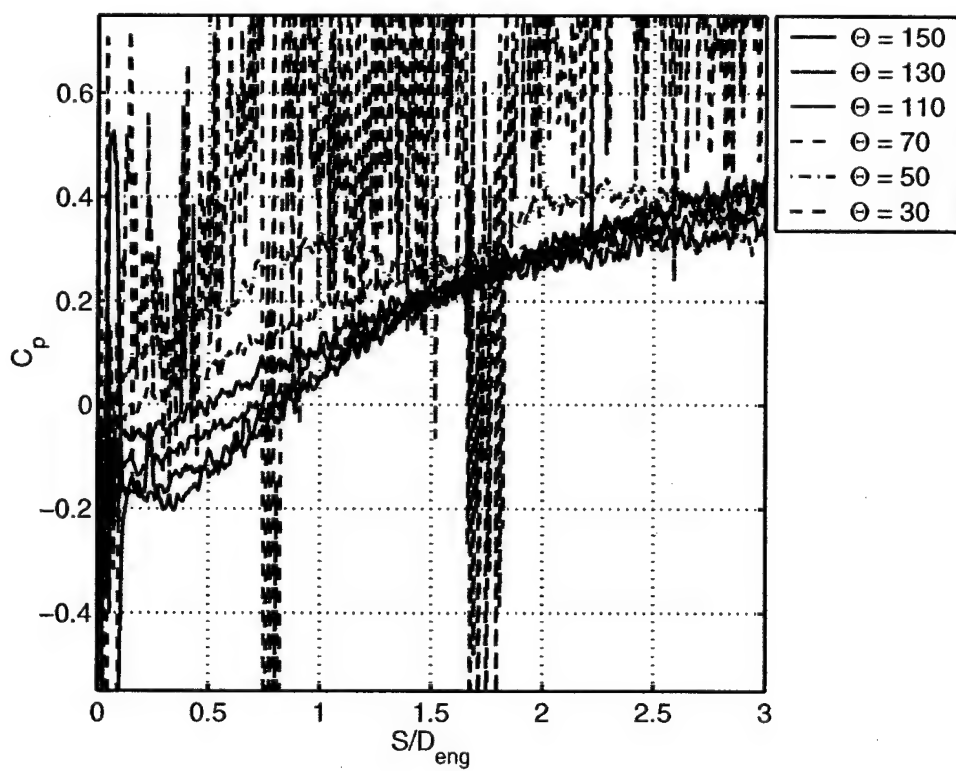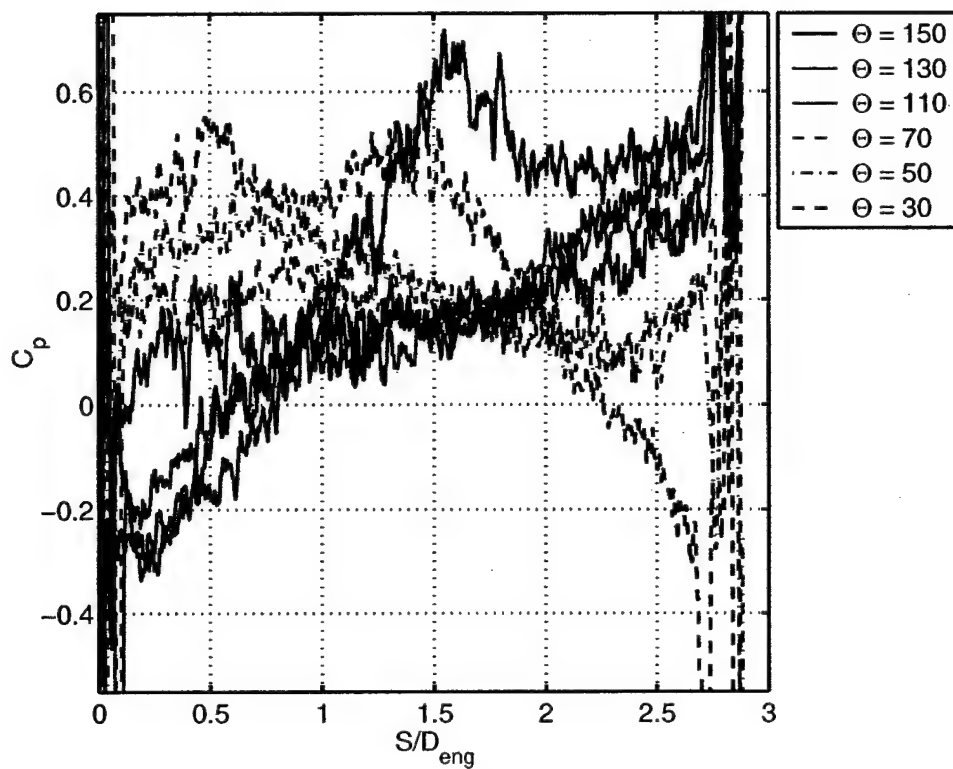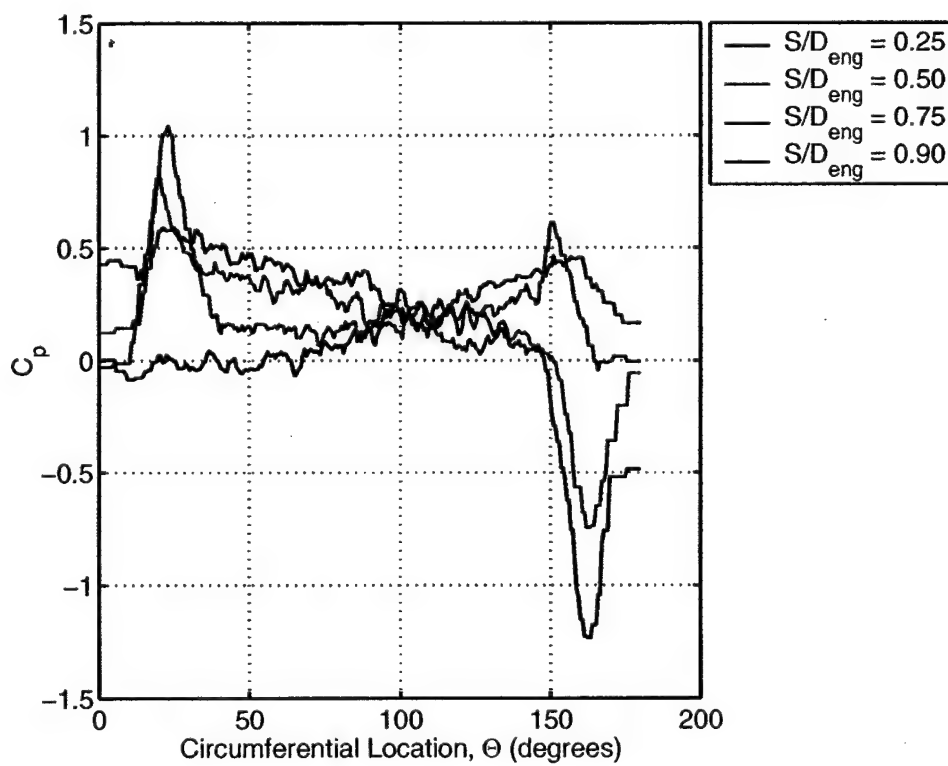
(a)Axial Distribution of Cp
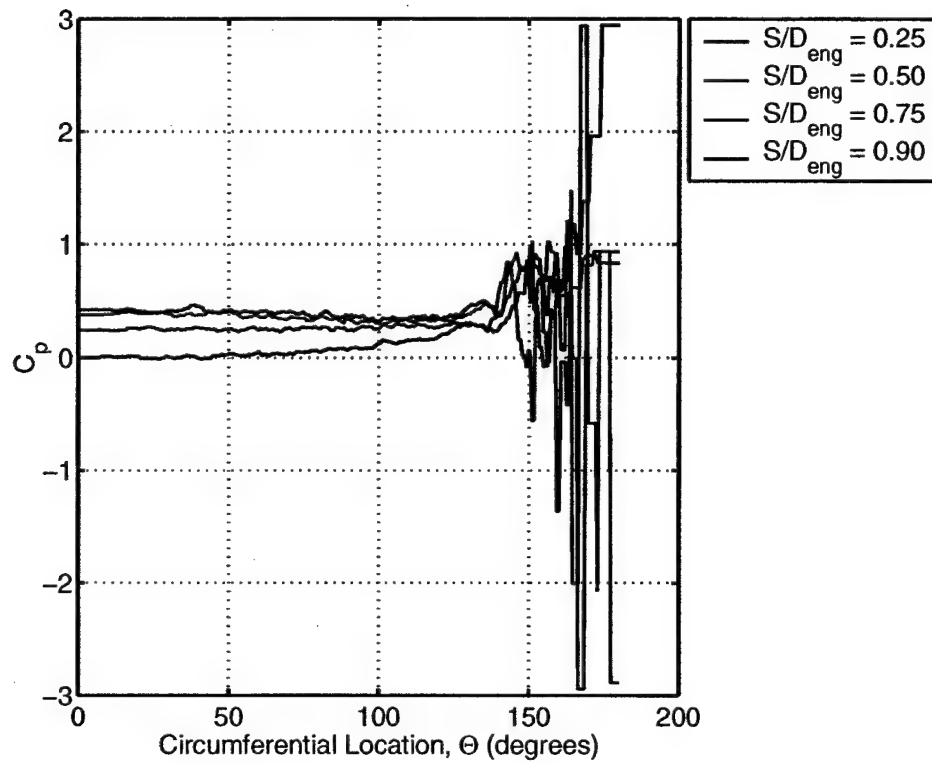
(a)Circumferential Distribution of Cp

Figure 32. PSP Data for M2129L with 1D Tangent at Mach = 0.6
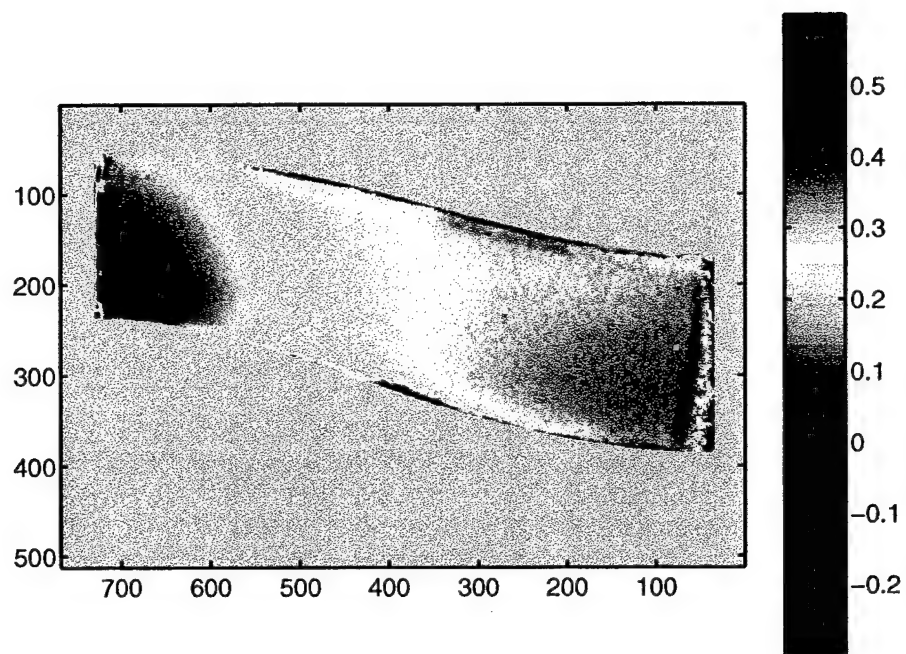
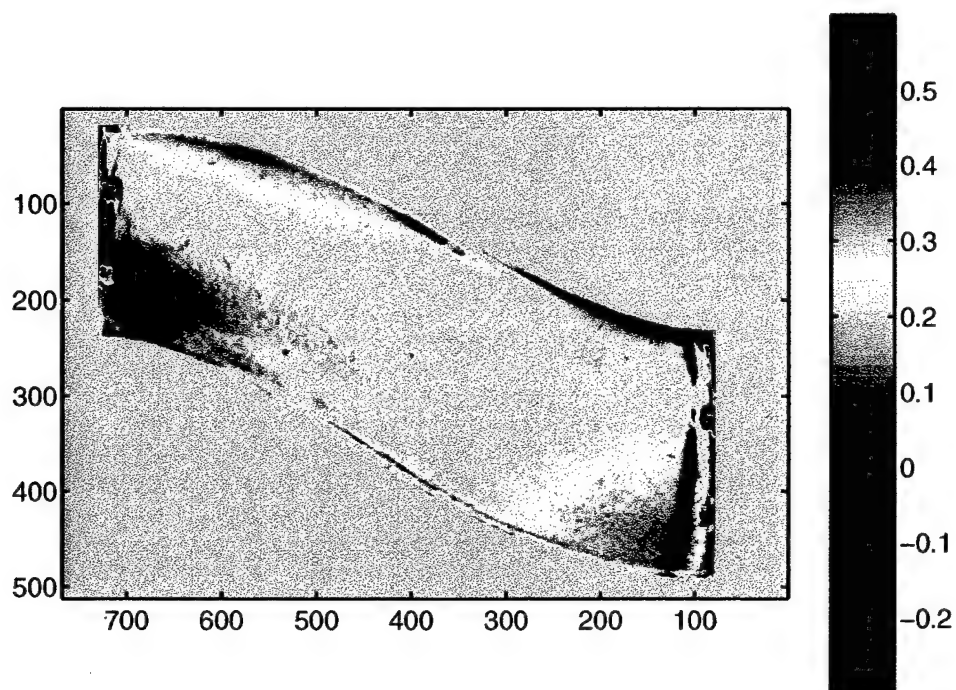**Figure 33. Mapping for M2129L with 1D Tangent at Mach = 0.8**
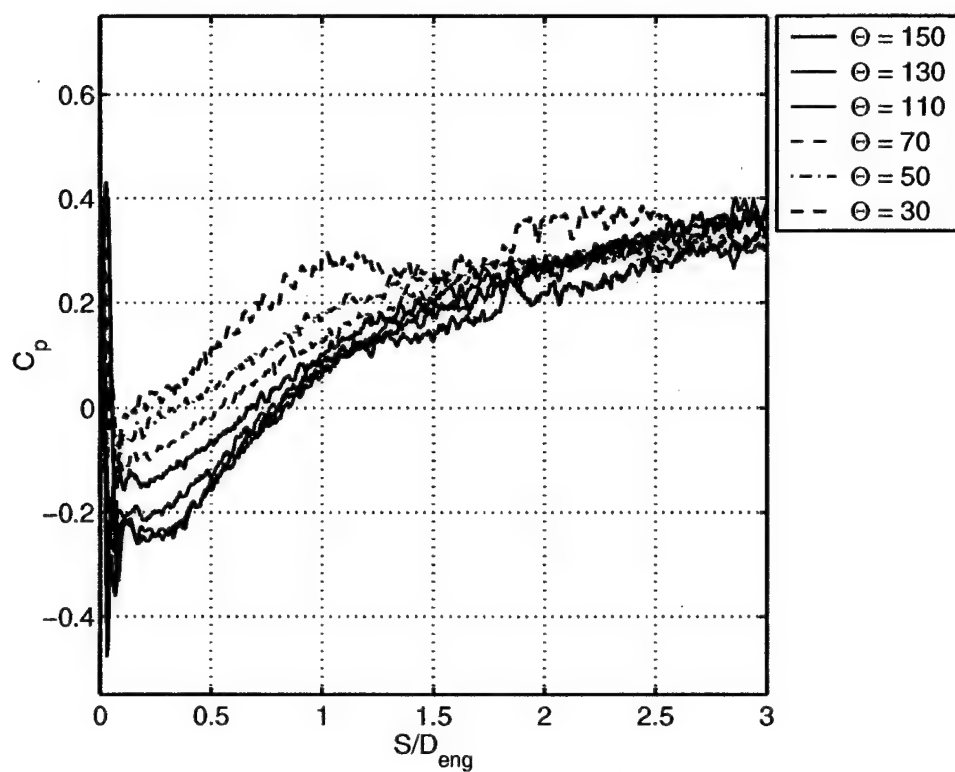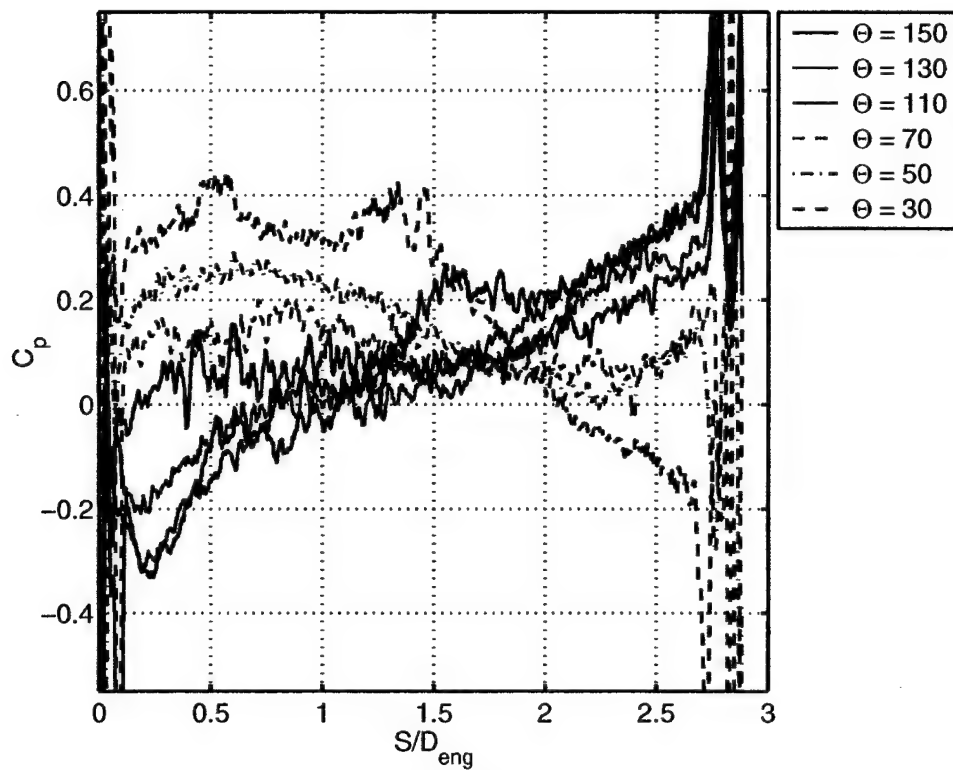
Axial Distribution of Cp

(a)
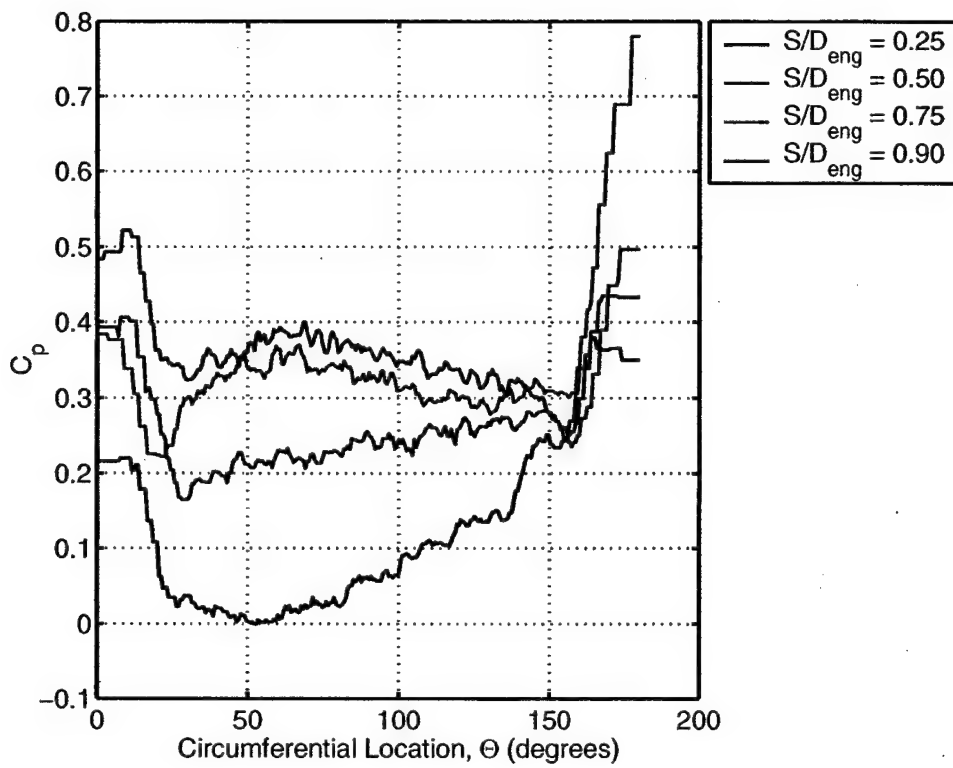
(a)Circumferential Distribution of Cp

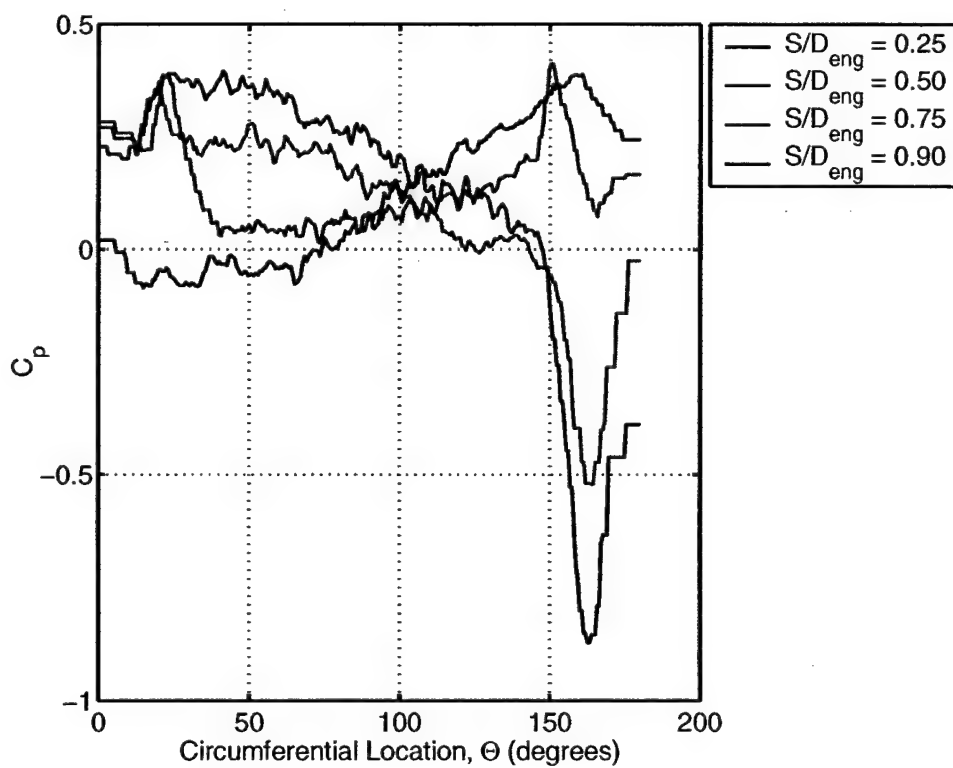**Figure 34. PSP Data for M2129L with 1D Tangent at Mach = 0.8**
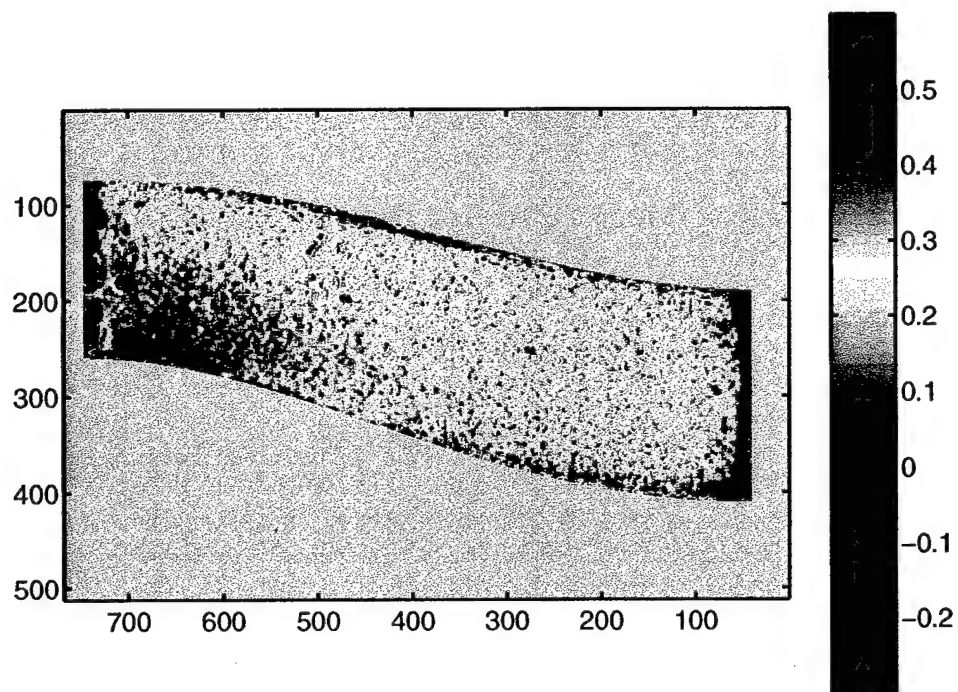
Figure 35. Mapping for M2129L with 2D Tangent at Mach = 0.2
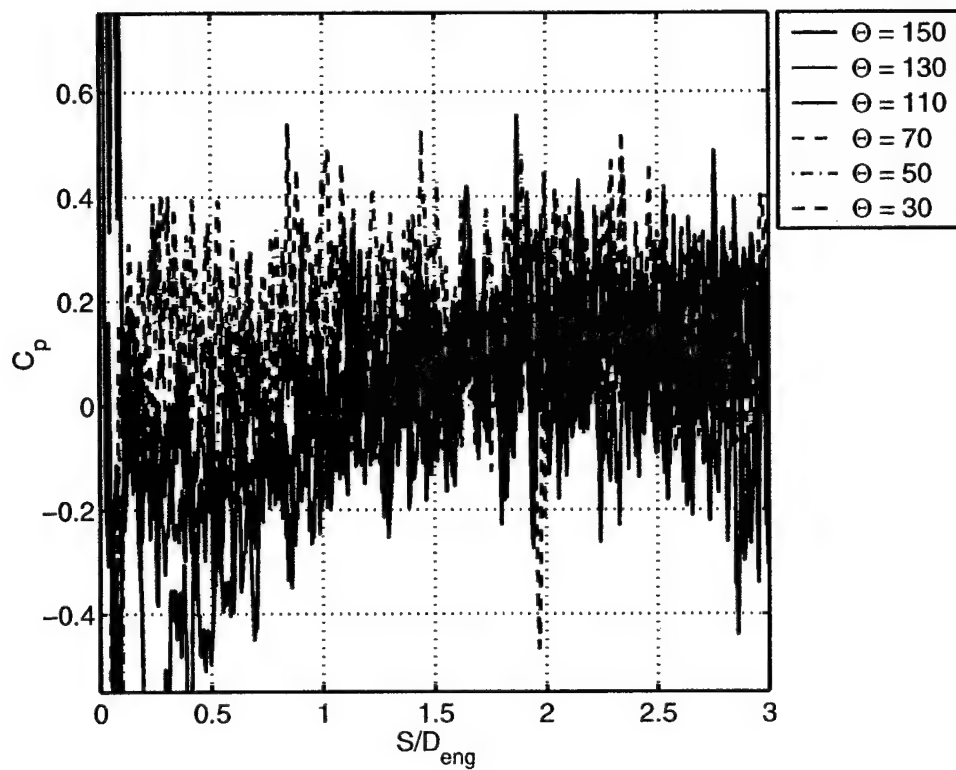
(a)Axial Distribution of Cp
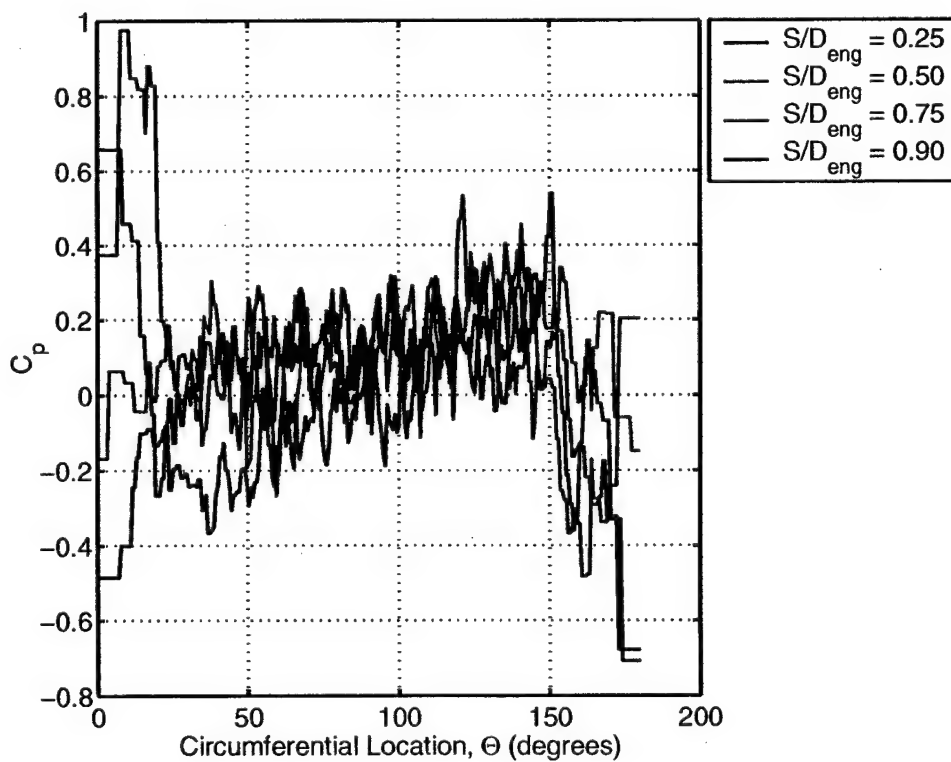
(a)Circumferential Distribution of Cp

Figure 36. PSP Data for M2129L with 2D Tangent at Mach = 0.2
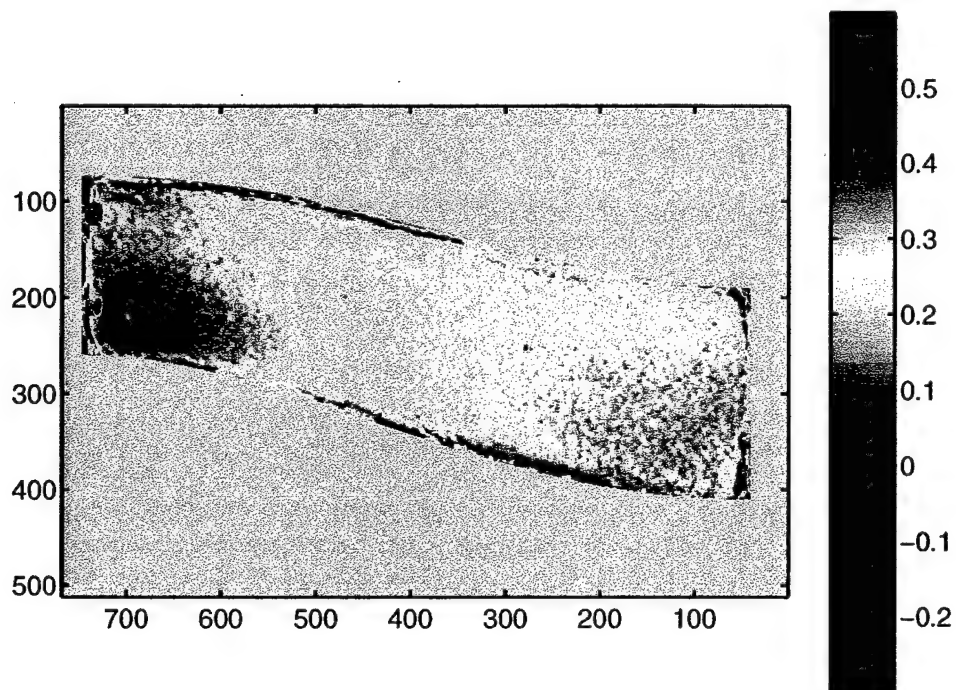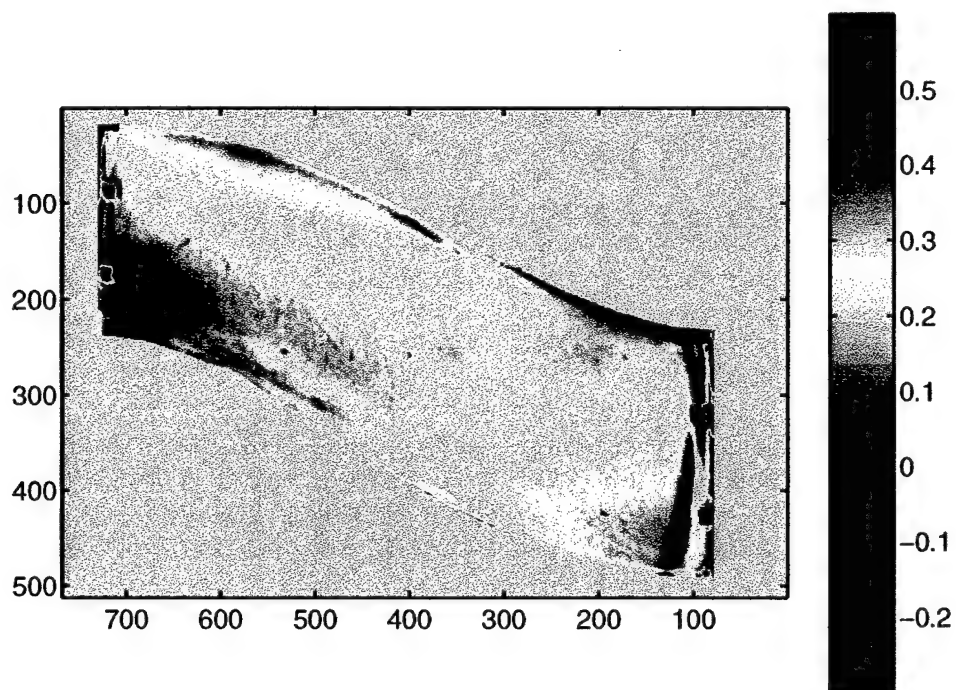
Figure 37. Mapping for M2129L with 2D Tangent at Mach = 0.4
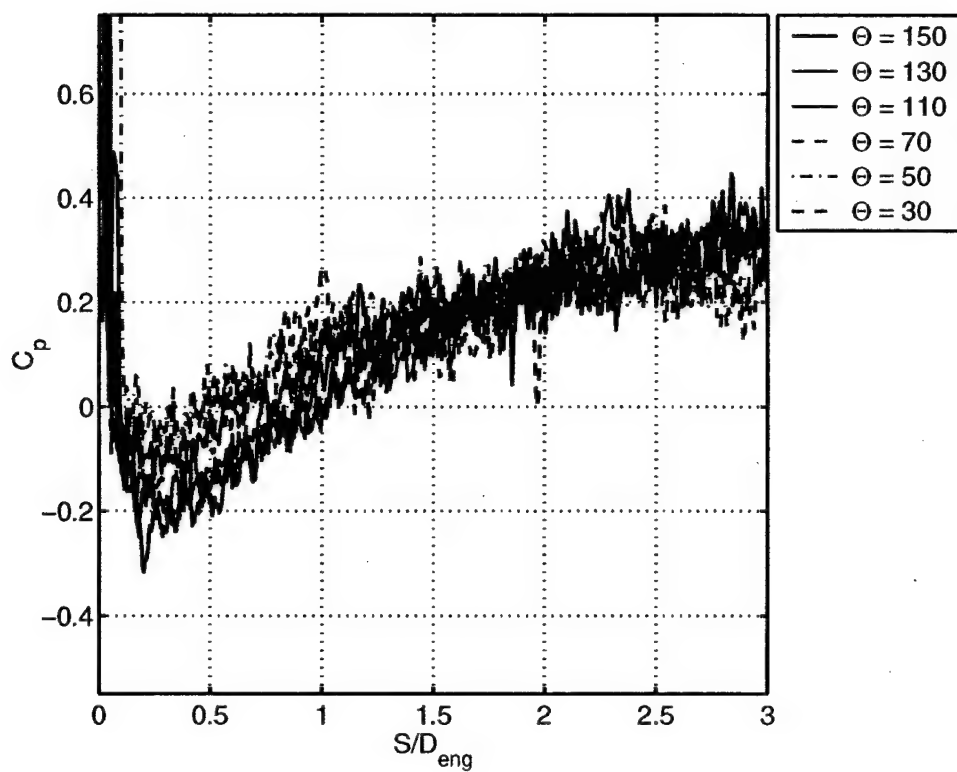
(a)Axial Distribution of Cp
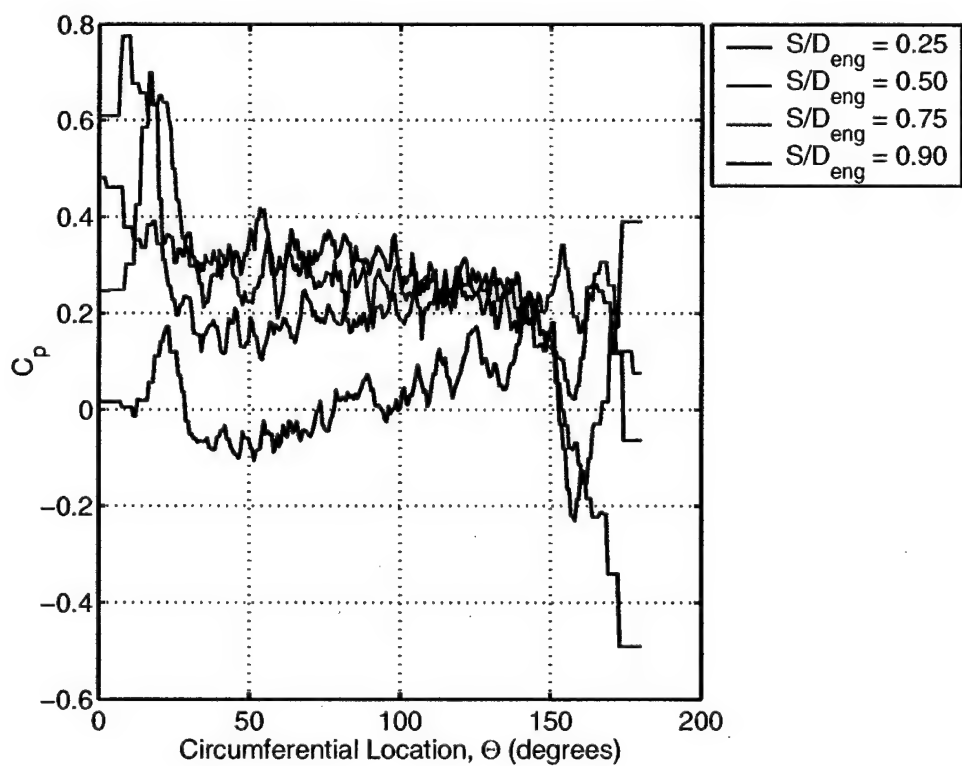
(a)Circumferential Distribution of Cp

Figure 38. PSP Data for M2129L with 2D Tangent at Mach = 0.4
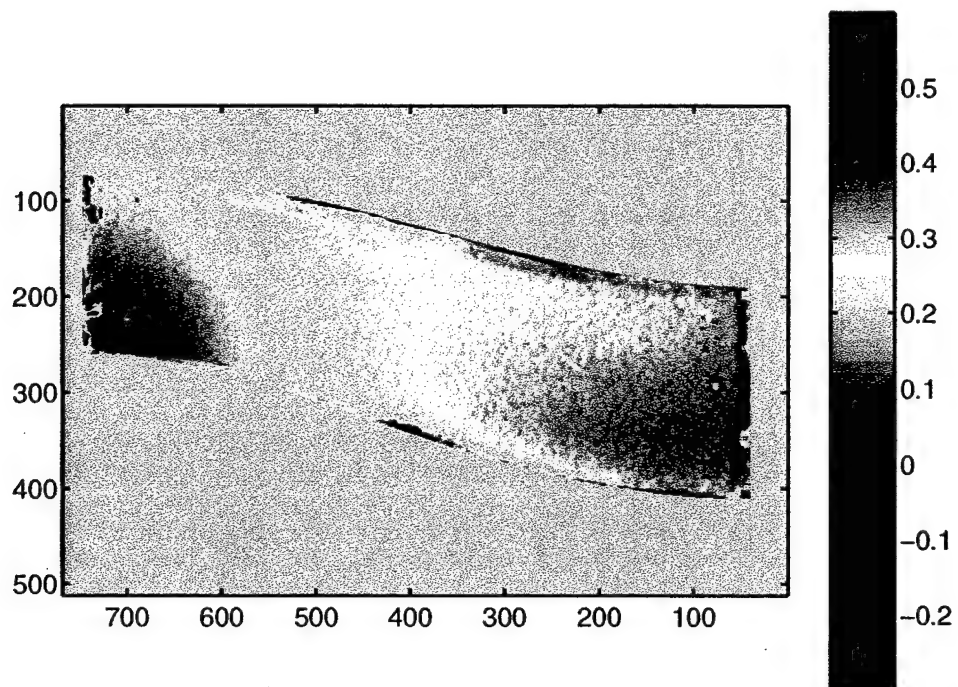
Figure 39. Mapping for M2129L with 2D Tangent at Mach = 0.6
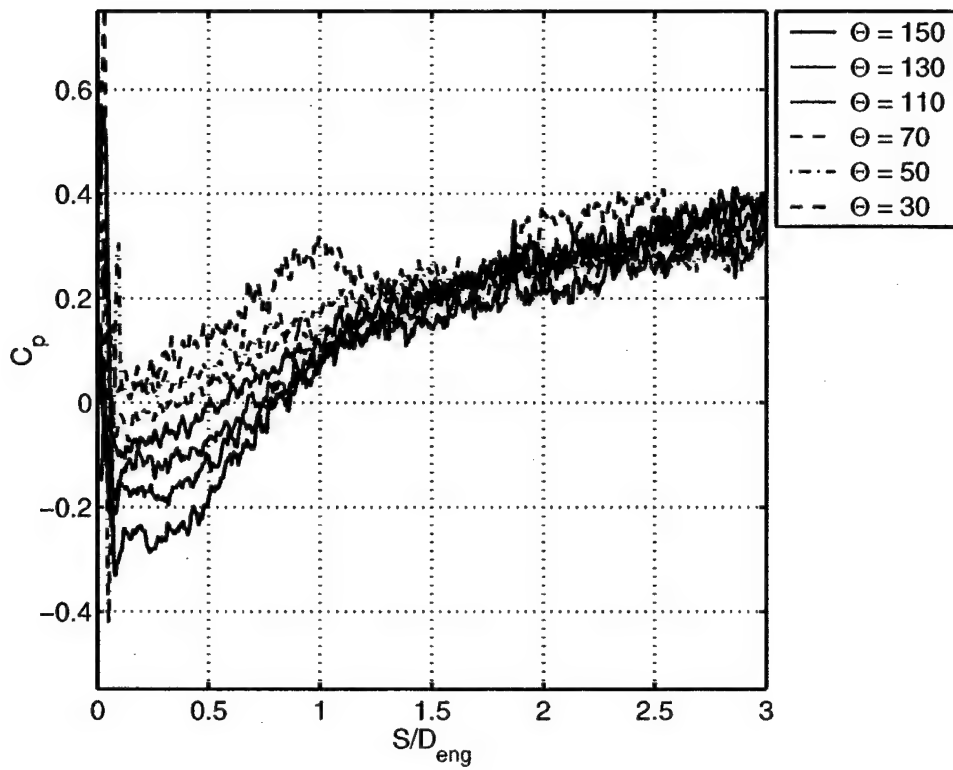
(a)Axial Distribution of Cp
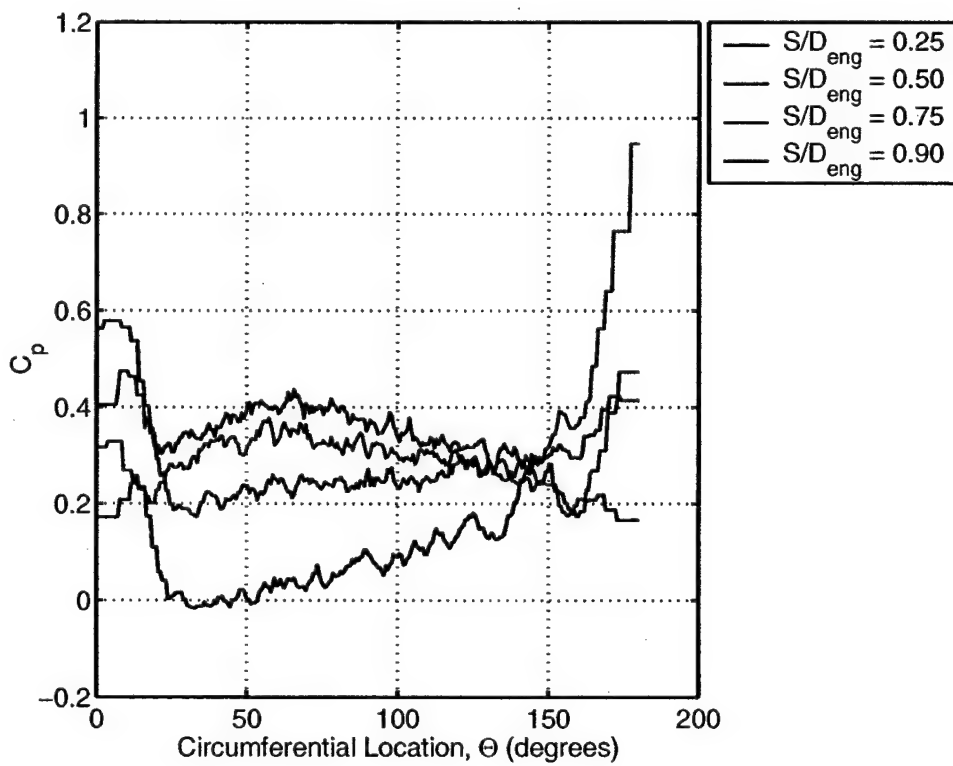
(b)Circumferential Distribution of Cp

Figure 40. PSP Data for M2129L with 2D Tangent at Mach = 0.6
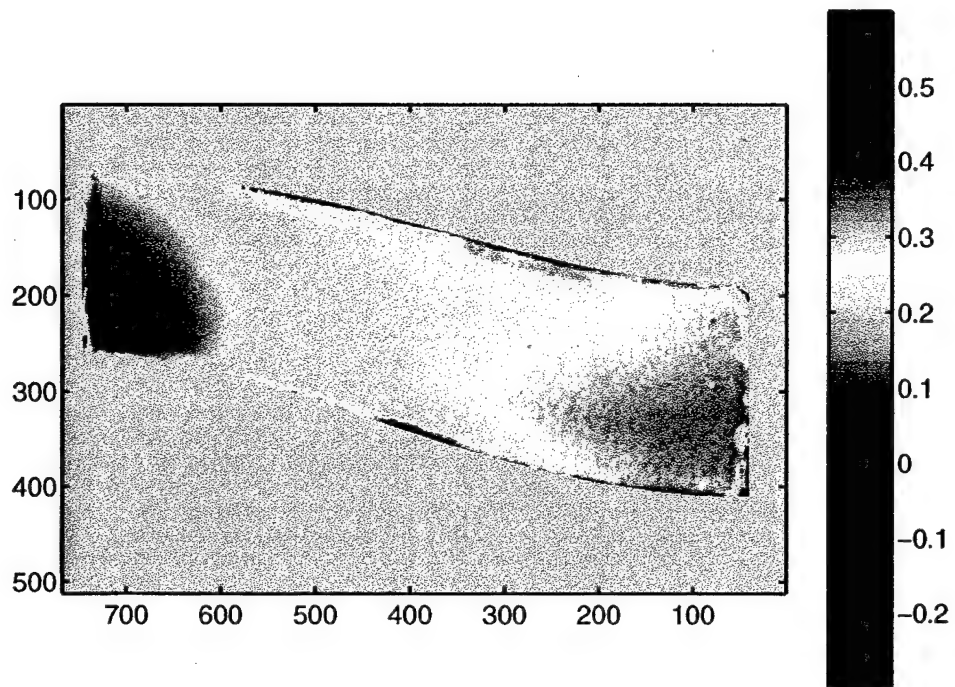
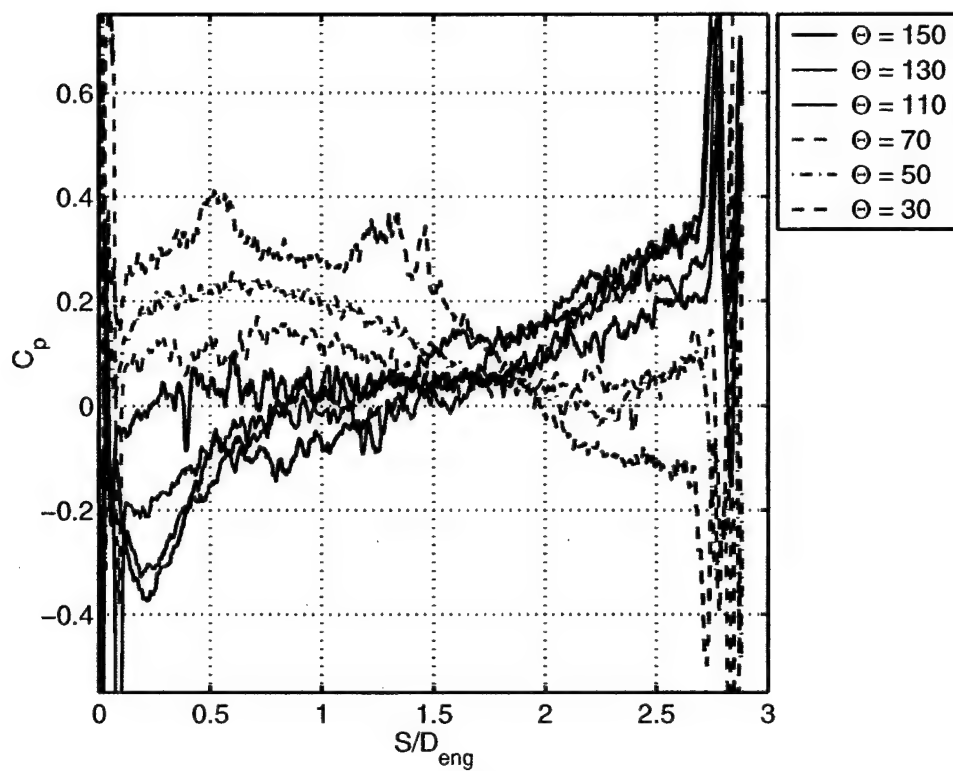Figure 41. Mapping for M2129L with 2D Tangent at Mach = 0.8
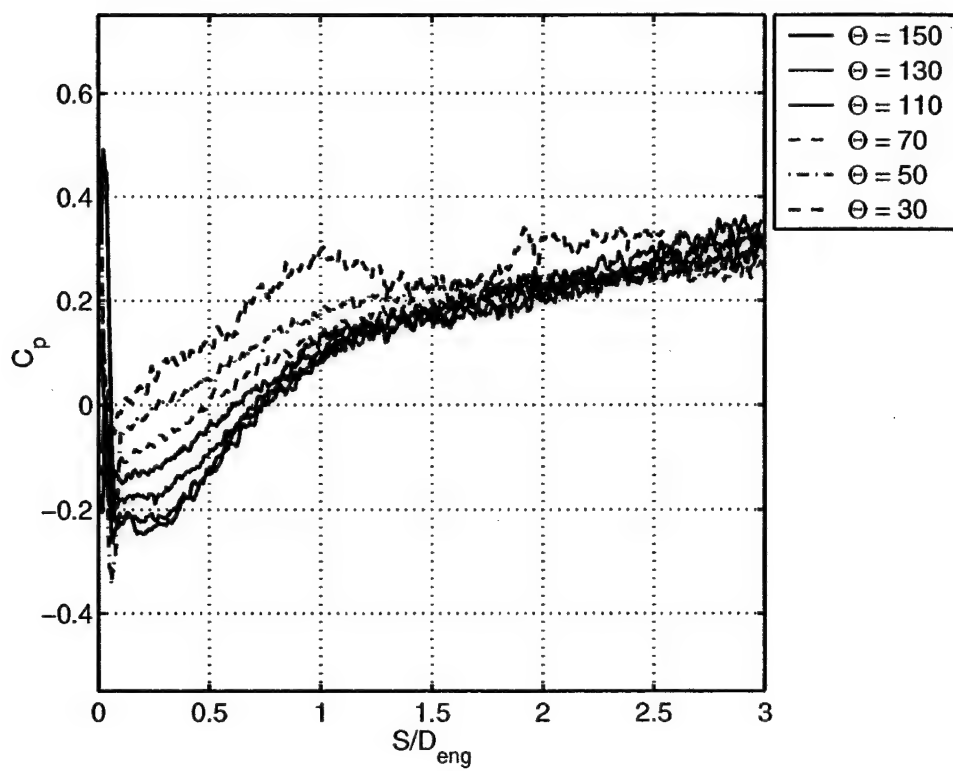
(a)Axial Distribution of Cp
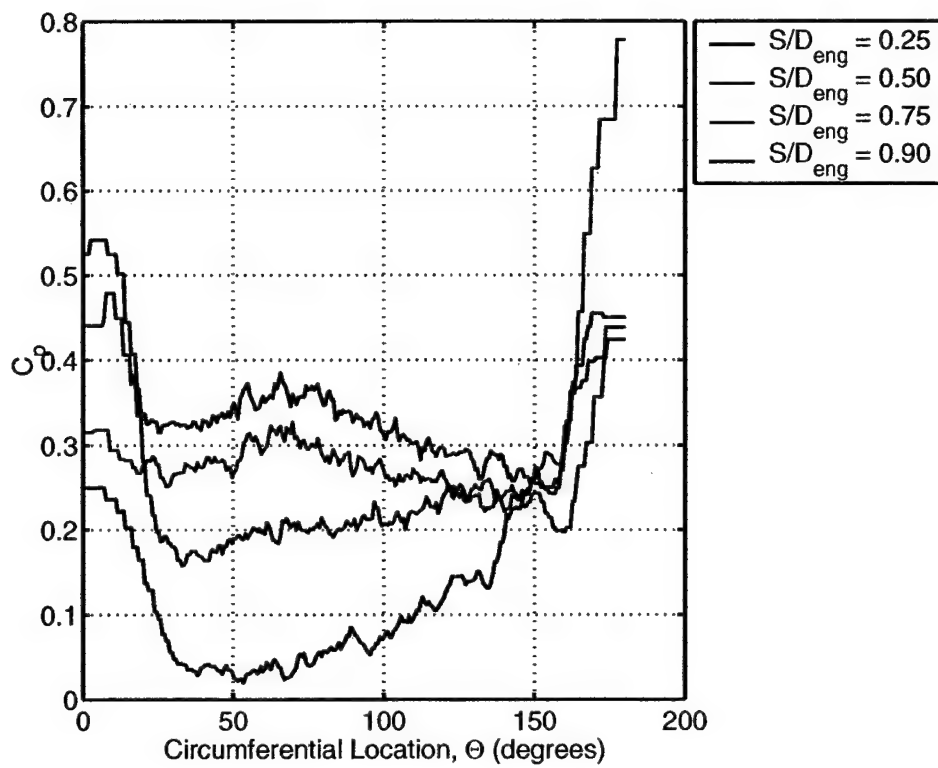
(b)Circumferential Distribution of Cp

Figure 42. PSP Data for M2129L with 2D Tangent at Mach = 0.8

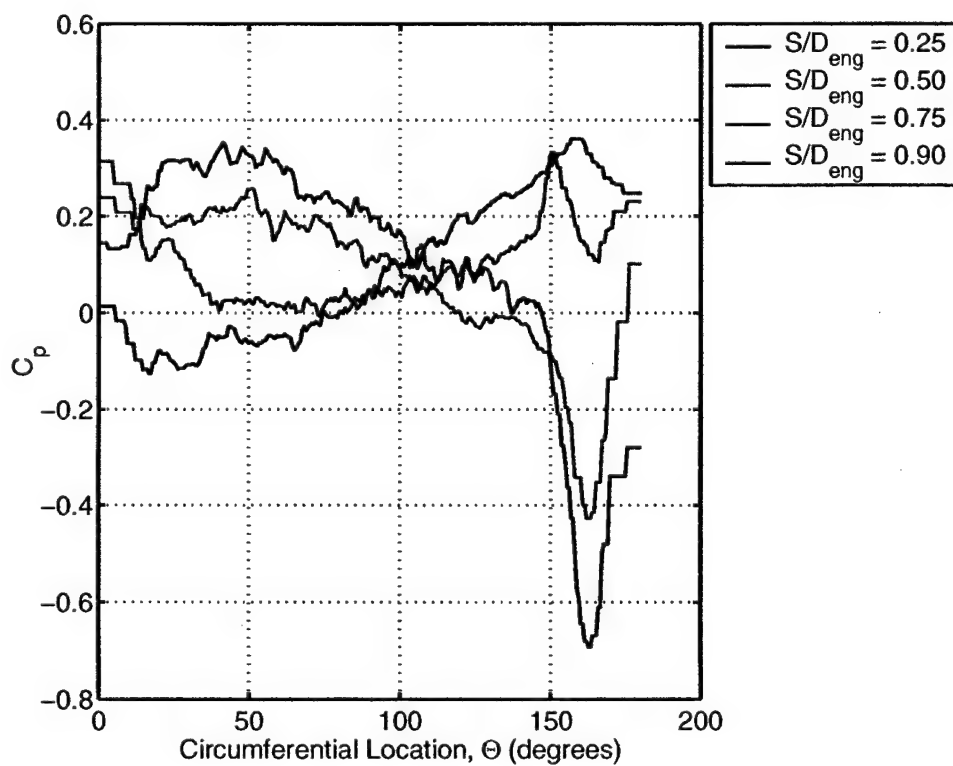## B. M2129S, Mach = 0.2-0.7
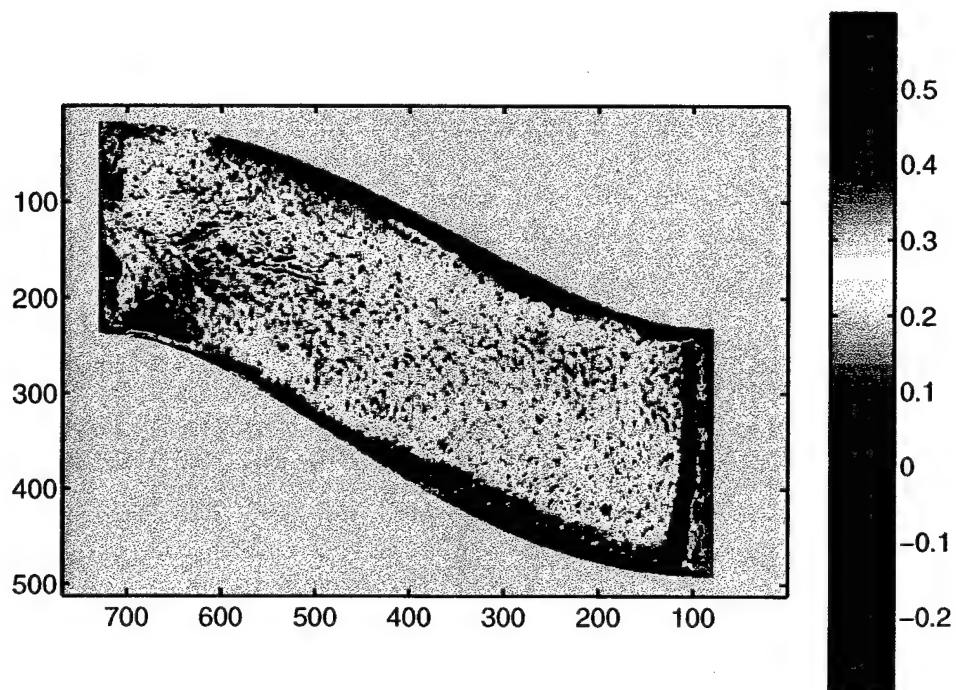
Figure 43. Mapping for M2129S with 1D Tangent at Mach = 0.2
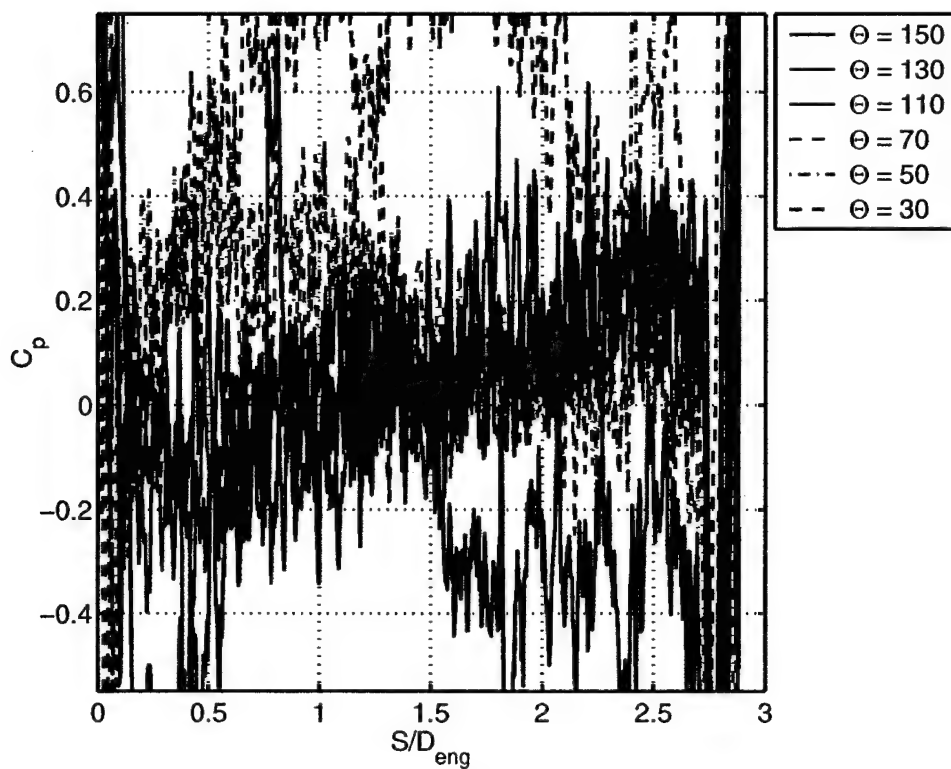
(a)Axial Distribution of Cp
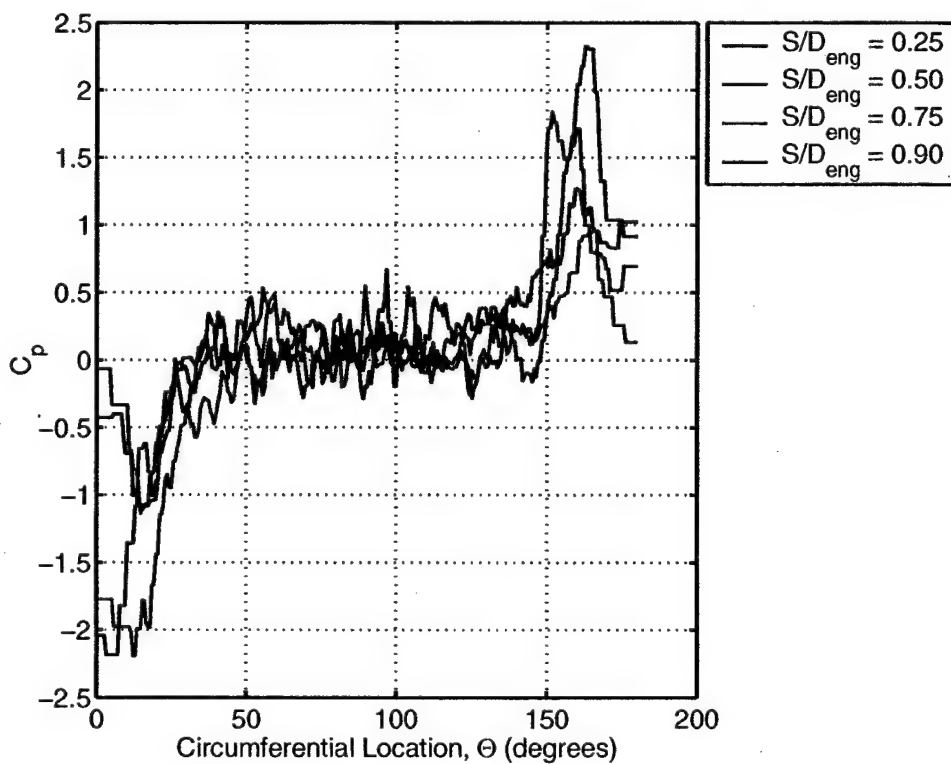
(b)Circumferential Distribution of Cp

Figure 44. PSP Data for M2129S with 1D Tangent at Mach = 0.2
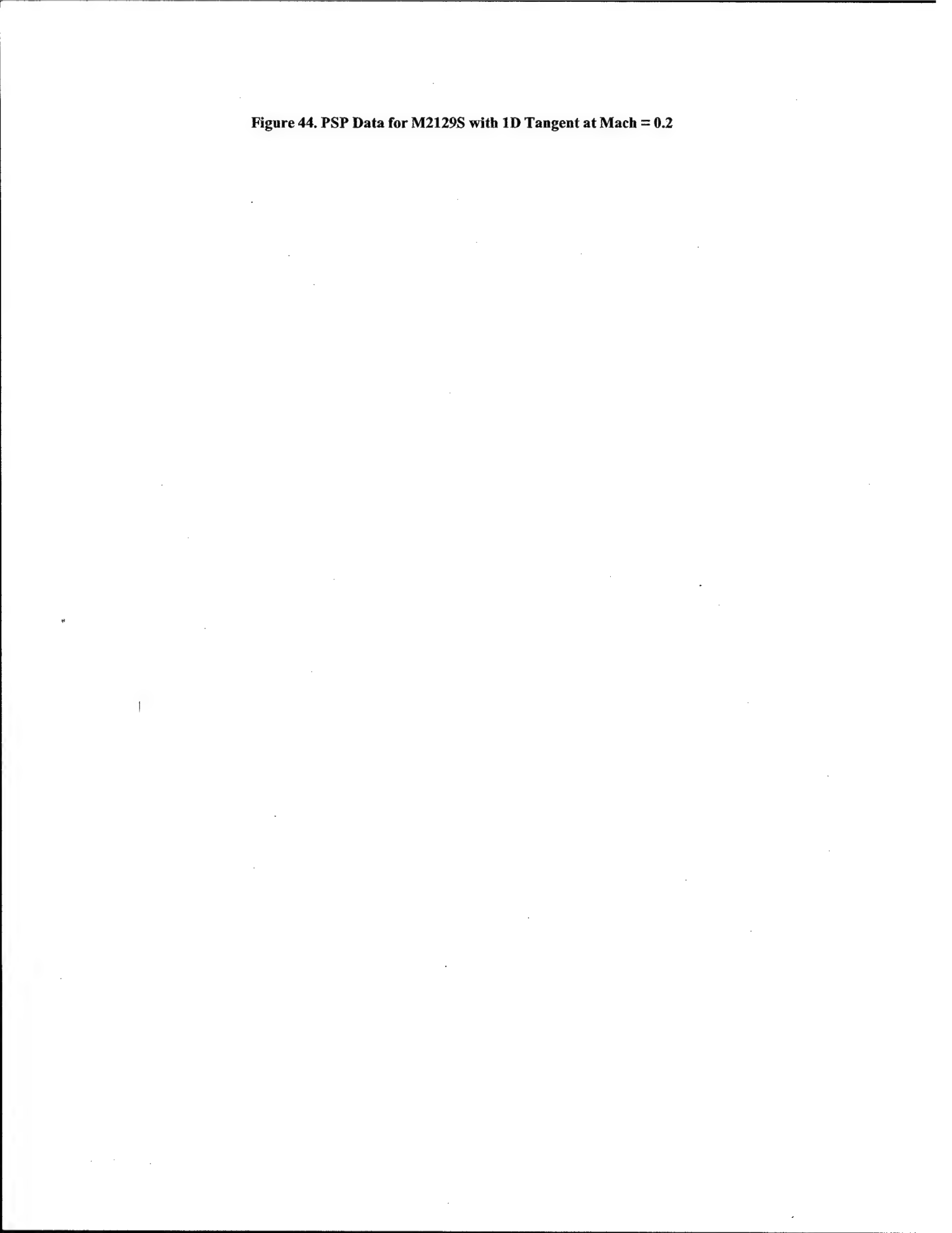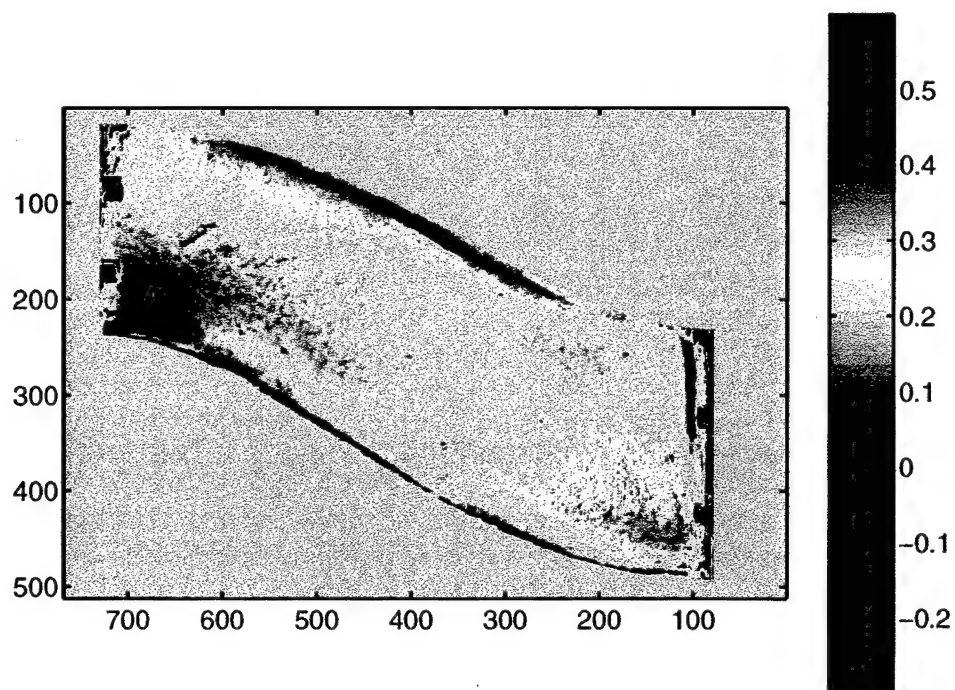
Figure 45. Mapping for M2129S with 1D Tangent at Mach = 0.4
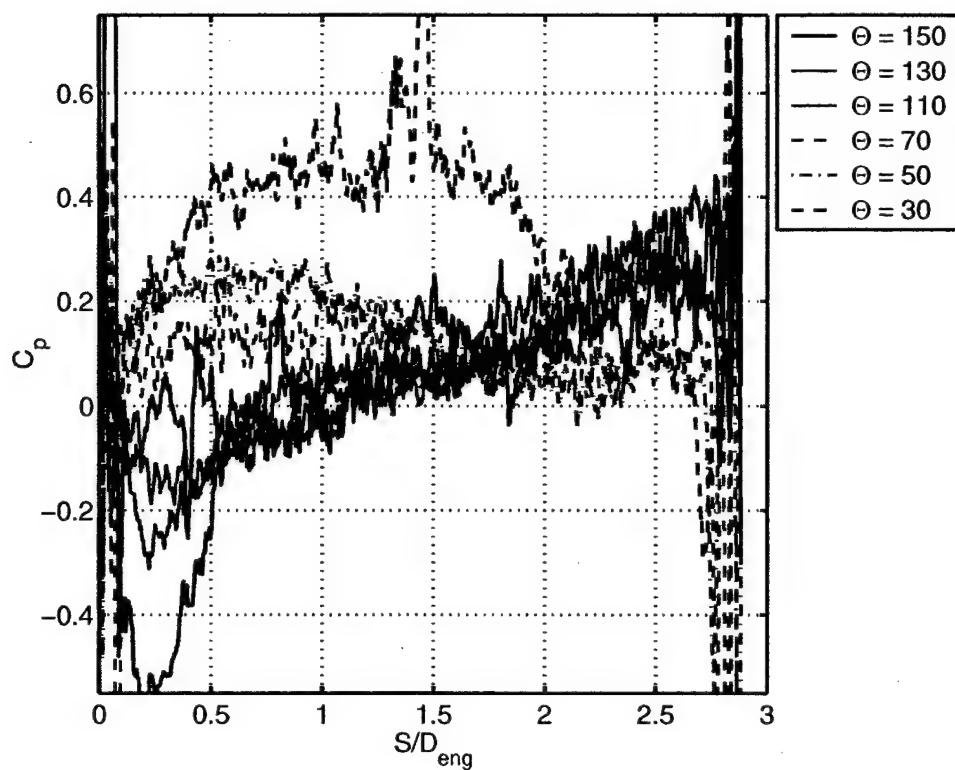
(a)Axial Distribution of Cp
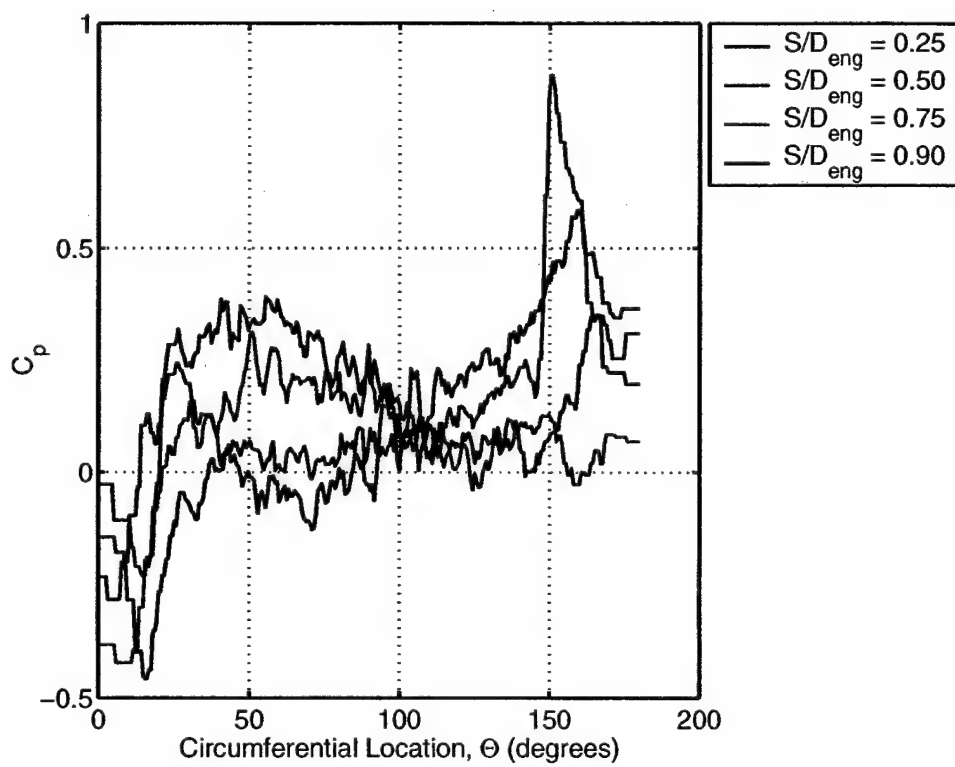
(b)Circumferential Distribution of Cp

Figure 46. PSP Data for M2129S with 1D Tangent at Mach = 0.4
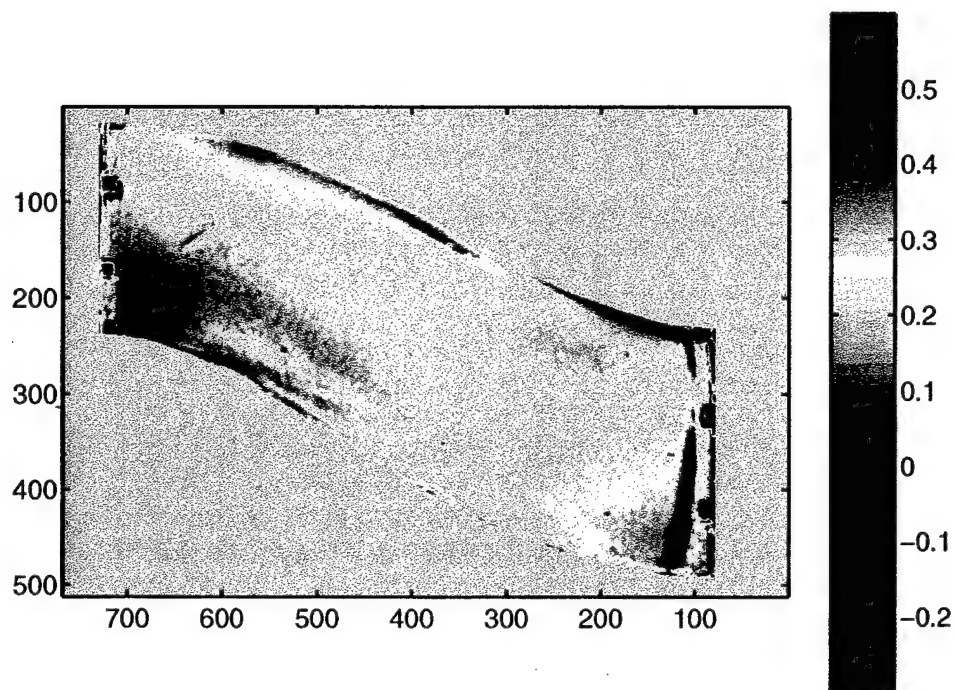
Figure 47. Mapping for M2129S with 1D Tangent at Mach = 0.6
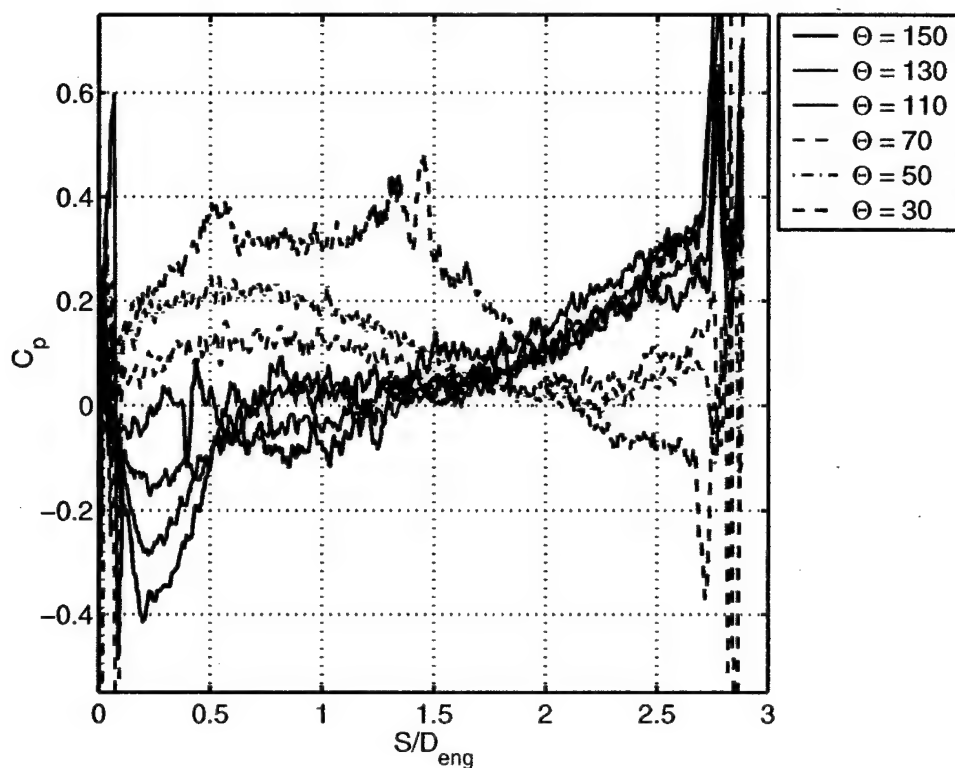
(a)Axial Distribution of Cp
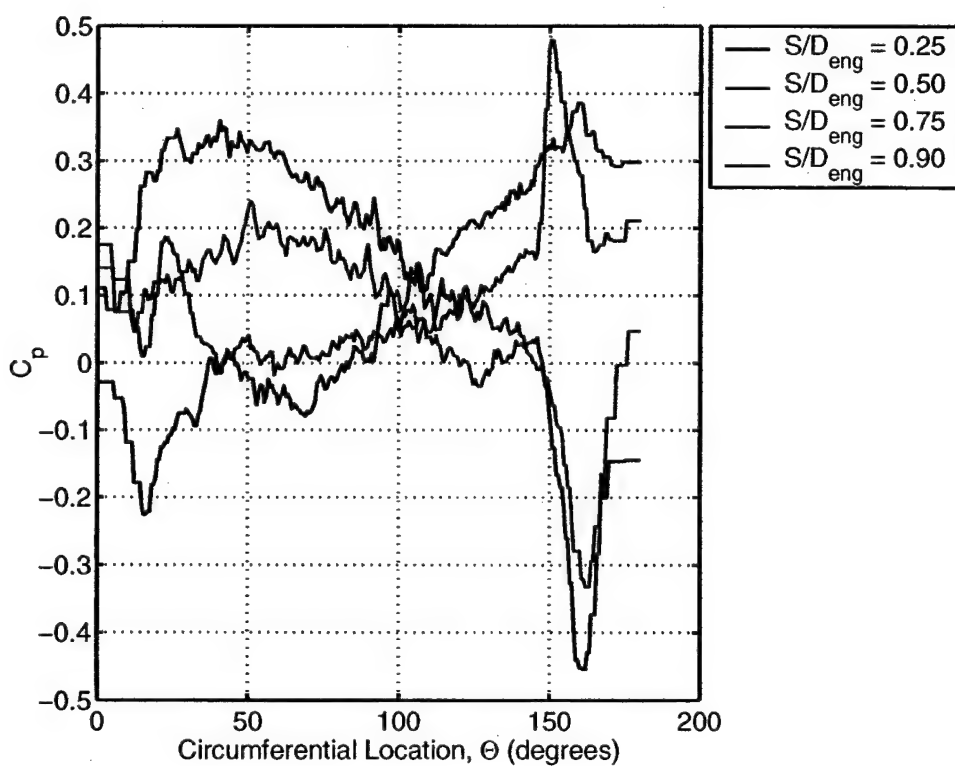
(b)Circumferential Distribution of Cp

Figure 48. PSP Data for M2129S with 1D Tangent at Mach = 0.6

Figure 49. Mapping for M2129S with 1D Tangent at Mach = 0.7

(a)Axial Distribution of Cp

(b)Circumferential Distribution of Cp

Figure 50. PSP Data for M2129S with 1D Tangent at Mach = 0.7

Figure 51. Mapping for M2129S with 2D Tangent at Mach = 0.2

(a)Axial Distribution of Cp

(b)Circumferential Distribution of Cp

Figure 52. PSP Data for M2129S with 2D Tangent at Mach = 0.2

Figure 53. Mapping for M2129S with 2D Tangent at Mach = 0.4

(a)Axial Distribution of Cp

(b)Circumferential Distribution of Cp

Figure 54. PSP Data for M2129S with 2D Tangent at Mach = 0.4

Figure 55. Mapping for M2129S with 2D Tangent at Mach = 0.6

(a)Axial Distribution of Cp

(b)Circumferential Distribution of Cp

Figure 56. PSP Data for M2129S with 2D Tangent at Mach = 0.6

Figure 57. Mapping for M2129S with 2D Tangent at Mach = 0.7

(a)Axial Distribution of Cp

(b)Circumferential Distribution of Cp

Figure 58. PSP Data for M2129S with 2D Tangent at Mach = 0.7

7. PSP Bulk Data

A. M2129L, Mach = 0.2-0.8
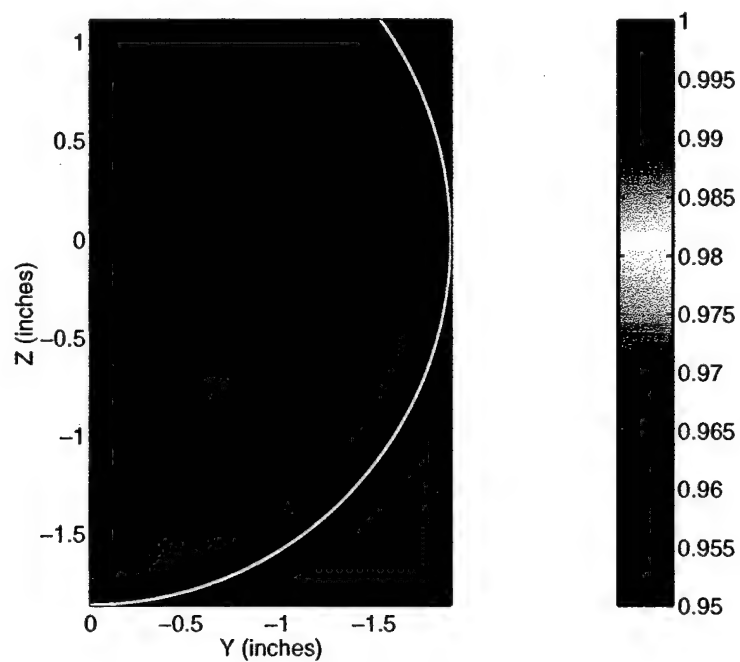
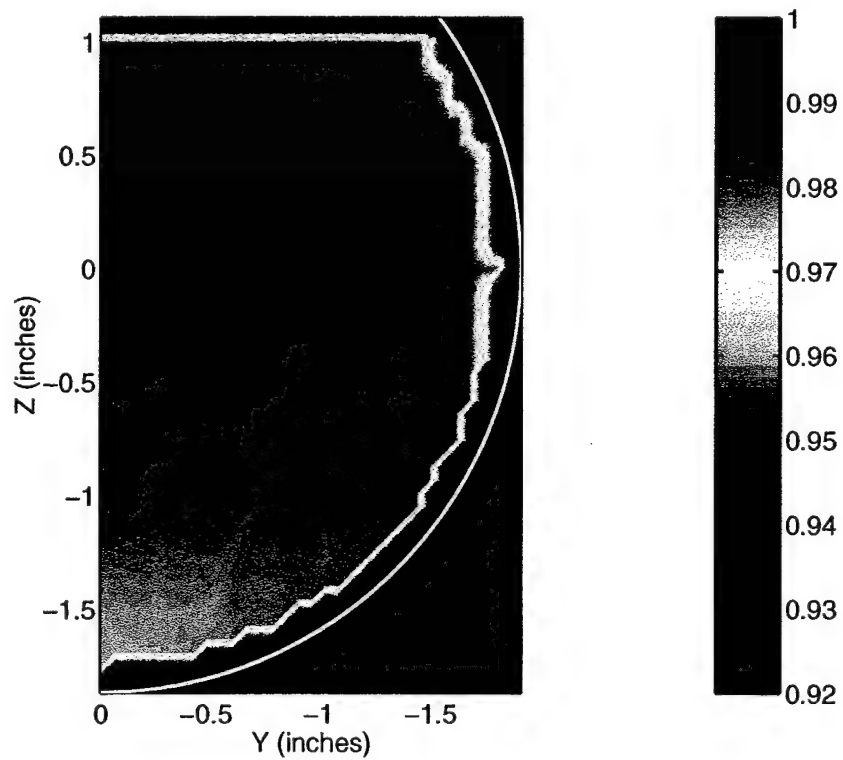**Figure 59. Total Pressure Loss at Engine Face for M2129L with 1D Tangent at Mach = 0.2**
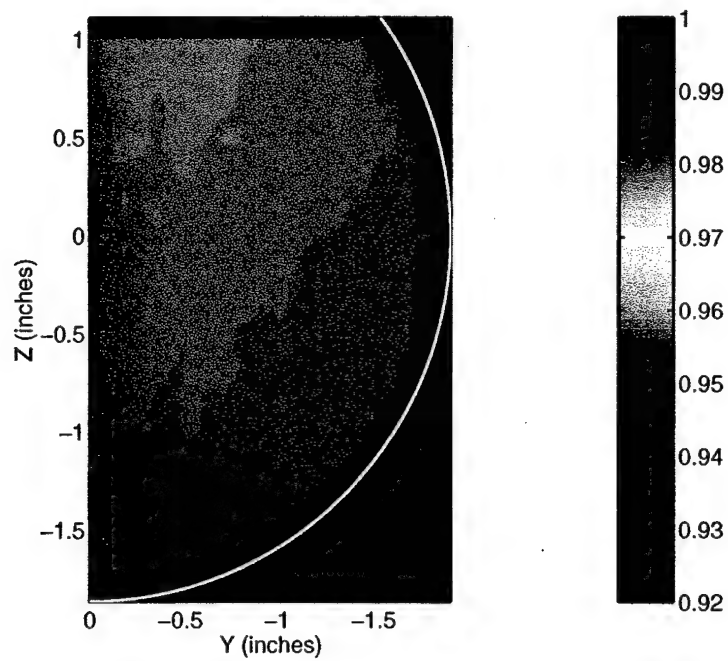
Figure 60. Static Pressure Ratio at Engine Face for M2129L with 1D Tangent at Mach = 0.2
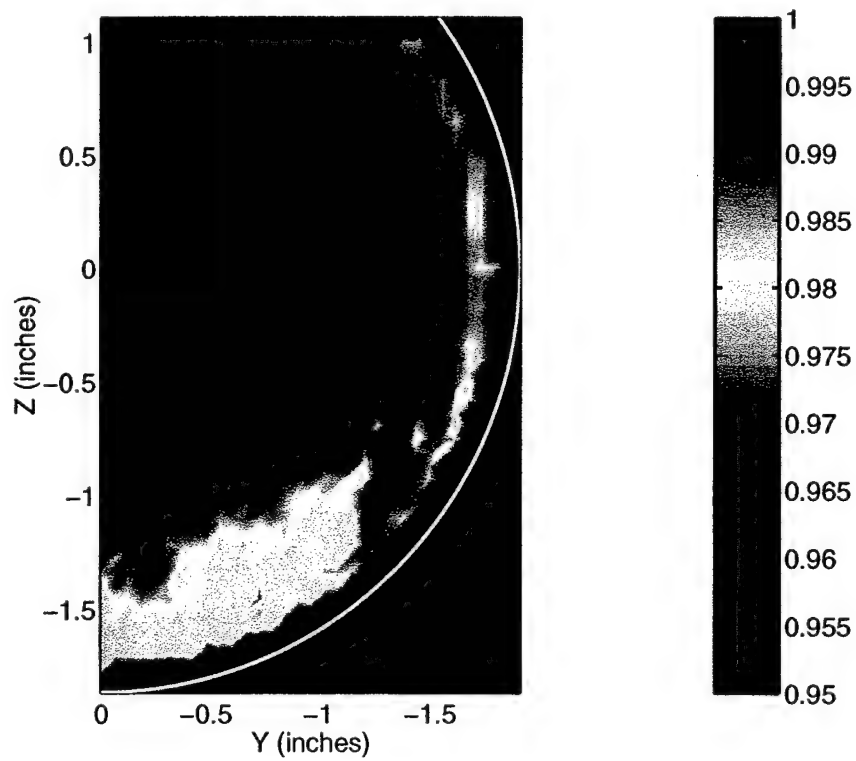
Figure 61. Total Pressure Loss at Engine Face for M2129L with 1D Tangent at Mach = 0.4
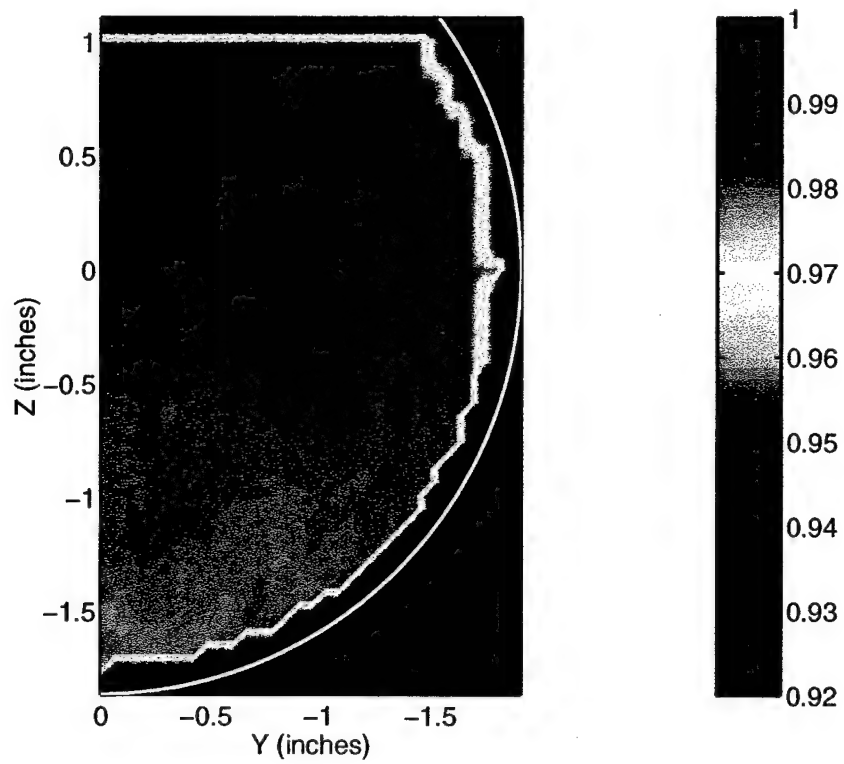
Figure 62. Static Pressure Ratio at Engine Face for M2129L with 1D Tangent at Mach = 0.4
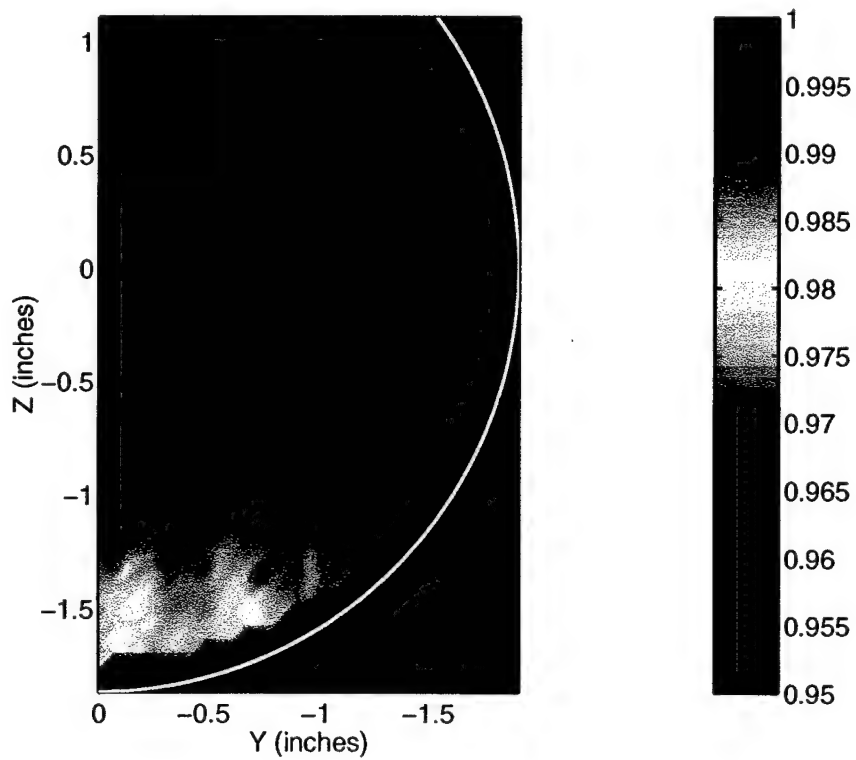
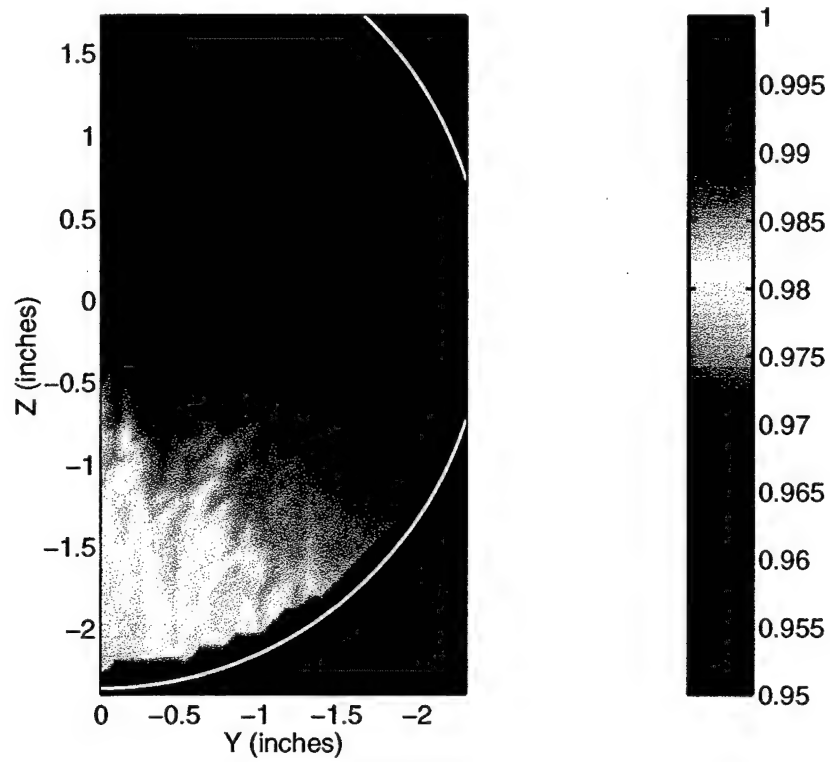**Figure 63. Total Pressure Loss at Engine Face for M2129L with 2D Tangent at Mach = 0.2**
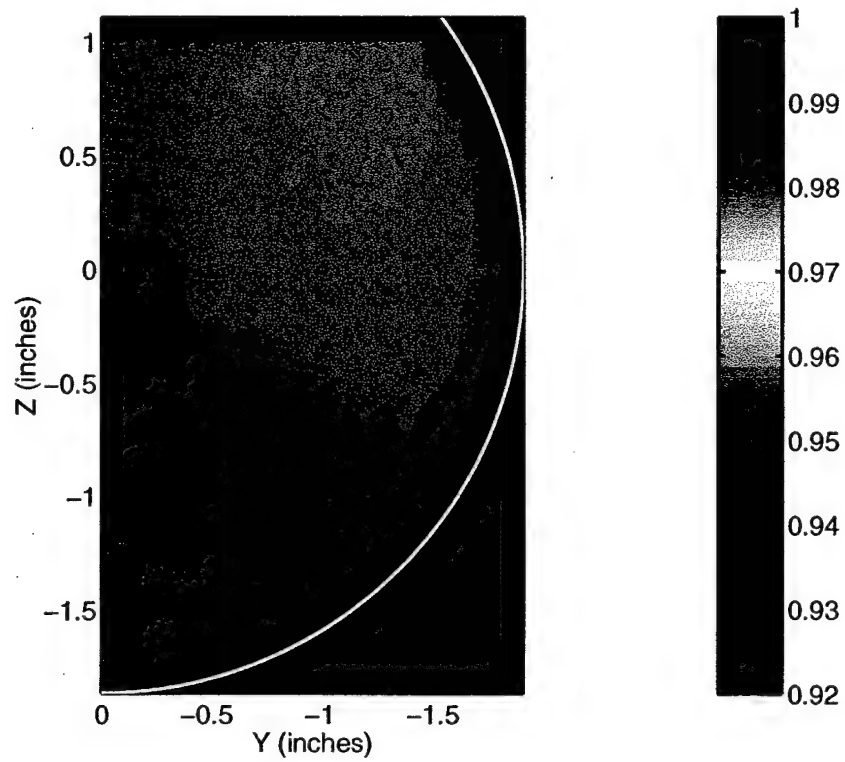
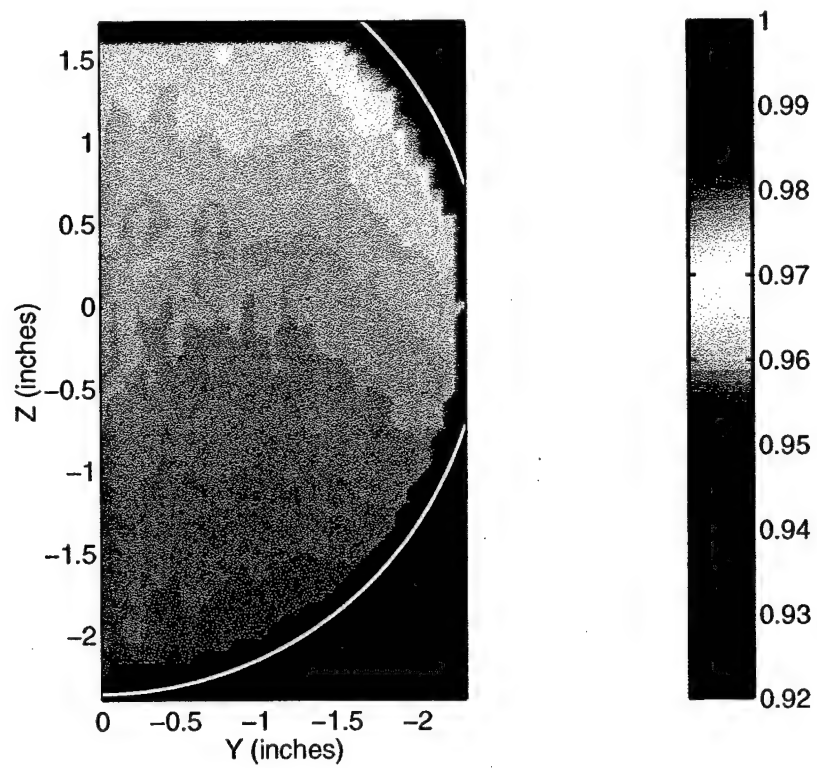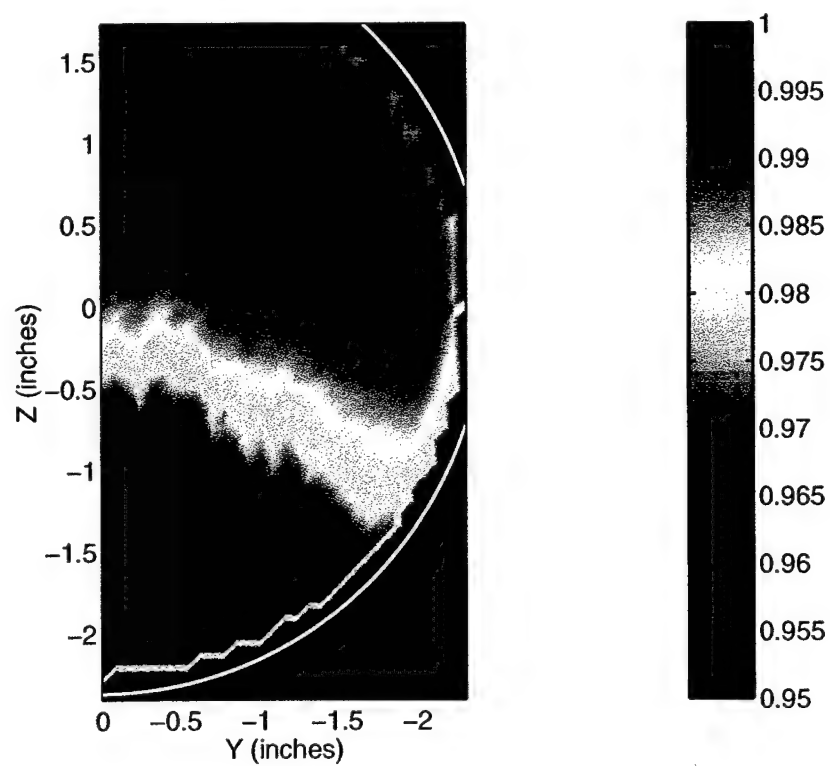**Figure 64. Static Pressure Ratio at Engine Face for M2129L with 2D Tangent at Mach = 0.2**
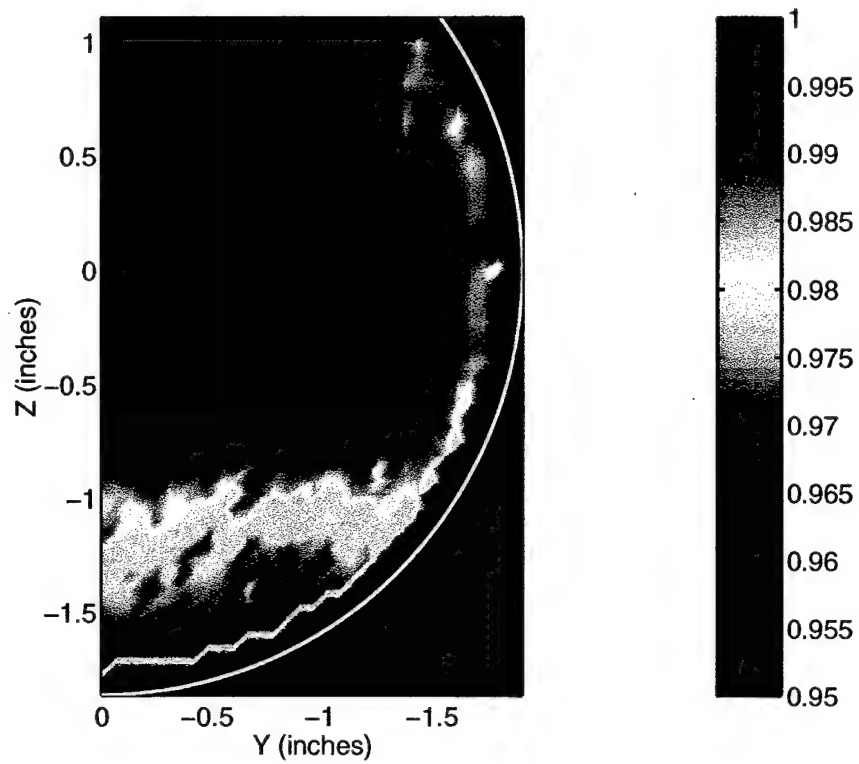
Figure 65. Total Pressure Loss at Engine Face for M2129L with 2D Tangent at Mach = 0.4

Figure 66. Static Pressure Ratio at Engine Face for M2129L with 2D Tangent at Mach = 0.4

B. M2129S

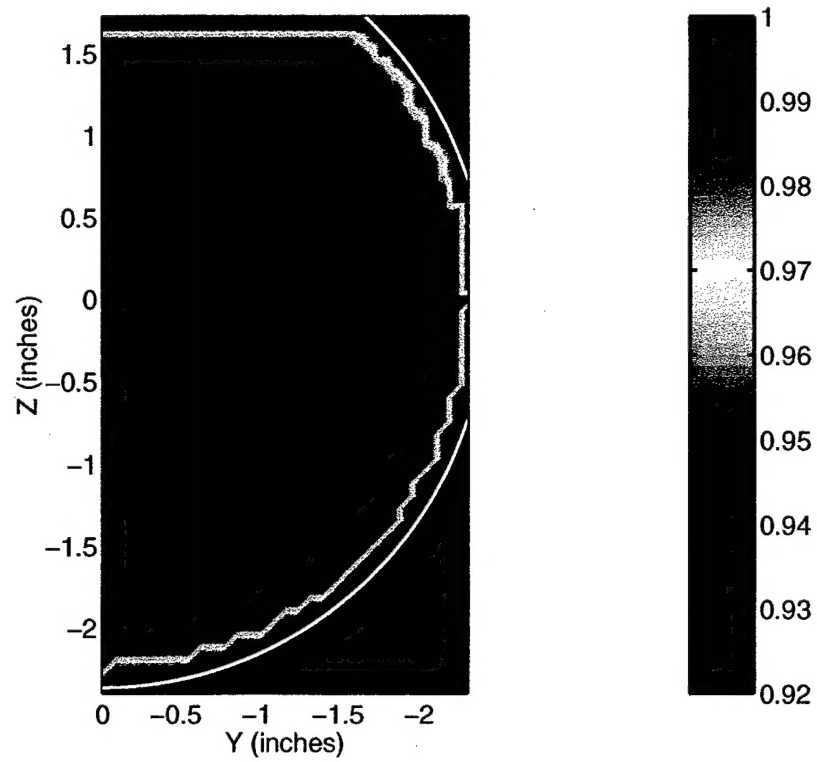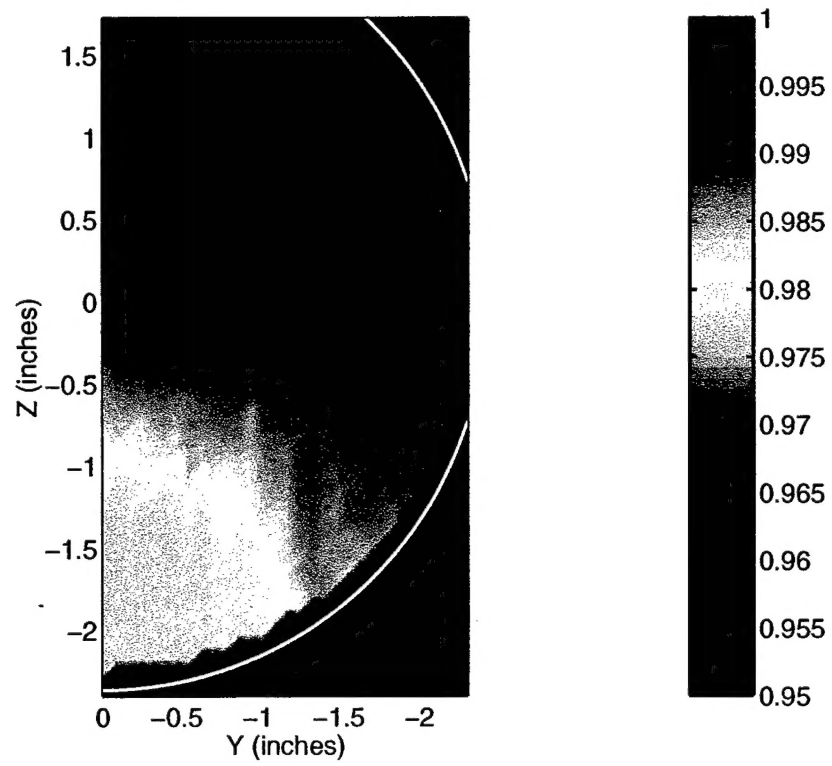**Figure 67. Total Pressure Loss at Engine Face for M2129S with 1D Tangent at Mach = 0.2**

Figure 68. Static Pressure Ratio at Engine Face for M2129S with 1D Tangent at Mach = 0.2
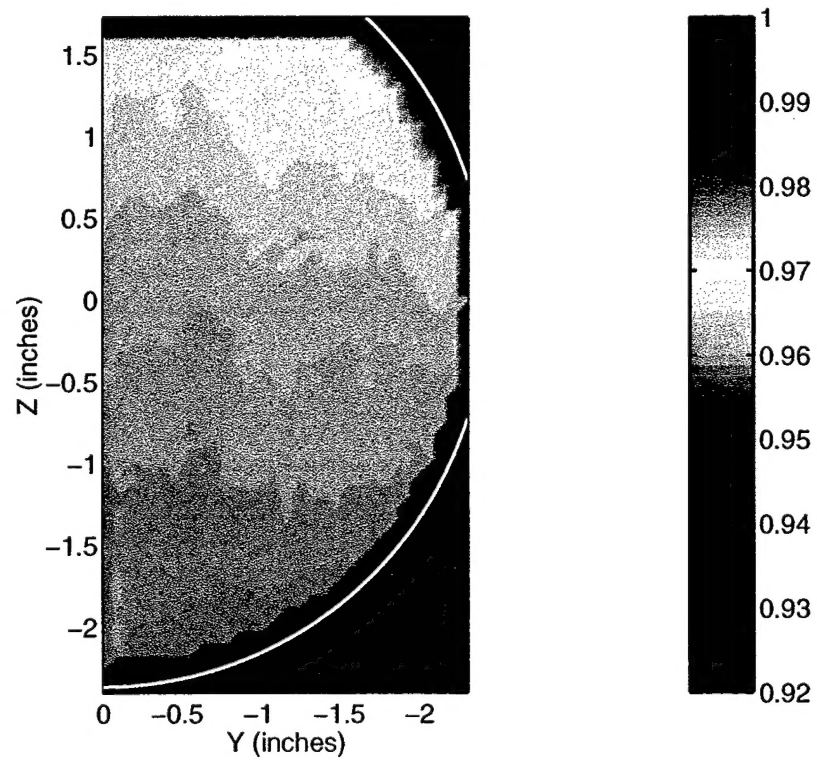
Figure 69. Total Pressure Loss at Engine Face for M2129S with 1D Tangent at Mach = 0.4
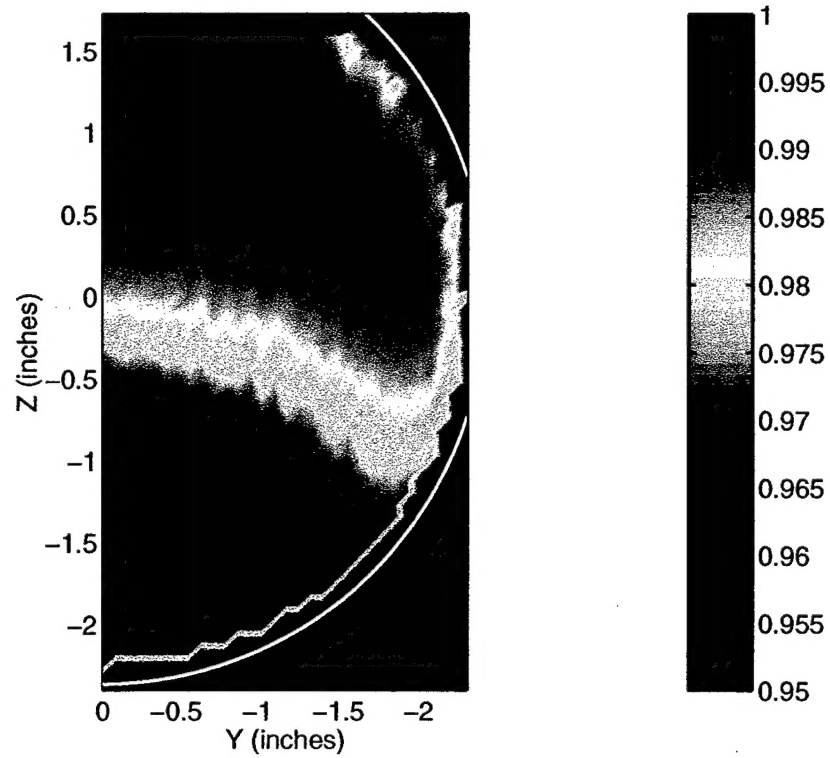

Figure 70. Static Pressure Ratio at Engine Face for M2129S with 1D Tangent at Mach = 0.4
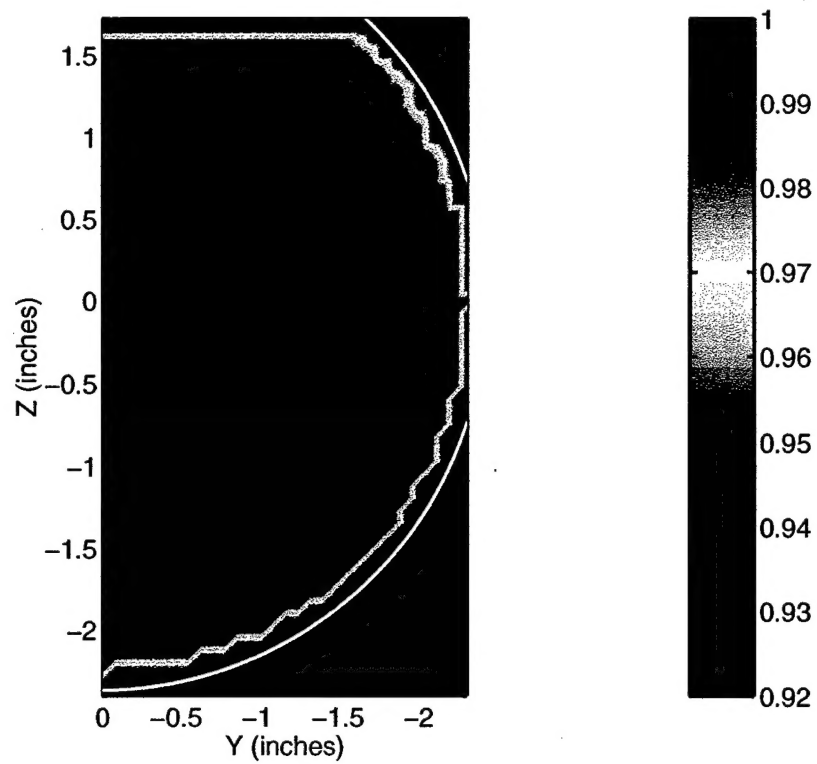
Figure 71. Total Pressure Loss at Engine Face for M2129S with 2D Tangent at Mach = 0.2

Figure 72. Static Pressure Ratio at Engine Face for M2129S with 2D Tangent at Mach = 0.2

Figure 73. Total Pressure Loss at Engine Face for M2129S with 2D Tangent at Mach = 0.4

Figure 74. Static Pressure Ratio at Engine Face for M2129S with 2D Tangent at Mach = 0.4